aerospace

MDPI

Article

Adaptive Neural Network-Based Sliding Mode Backstepping Control for Near-Space Morphing Vehicle

Shutong Huang [1,2,*], Ju Jiang [1] and Ouxun Li [1,2]

[1] College of Automation Engineering, Nanjing University of Aeronautics and Astronautics, Nanjing 211106, China; jiangju@nuaa.edu.cn (J.J.); liouxun@guat.edu.cn (O.L.)
[2] College of Electronic Information and Automation Engineering, Guilin University of Aerospace Technology, Guilin 541004, China
* Correspondence: huangshutong@nuaa.edu.cn; Tel.: +86-136-2783-2509

Abstract: In order to obtain good flight performance in the near-space morphing vehicle (NMV) cruise phase, this paper proposes an adaptive sliding mode backstepping control scheme based on a neural network, aiming at the reduction of elevator control efficiency and issues of uncertainties. Firstly, this paper analyzes the aerodynamic parameters of NMV in the states of winglet stretching and retracting during the cruise phase. Based on the above, the flight efficiency of NMV can be improved by retracting winglets in the level flight mode and stretching winglets in the altitude climbing mode. Secondly, an enhanced triple power reaching law (ETPRL) is proposed to ensure that the sliding mode control system can converge quickly and reduce chattering. Then, the sliding mode control based on ETPRL and backstepping control are combined to ensure the stability of the system, and adaptive control laws are developed to estimate and compensate for uncertainties. In addition, in face of the problem of reduced elevator control efficiency, the adaptive neural network is used to estimate and compensate for interference on the control channel to improve tracking accuracy and robustness of NMV. Finally, three sets of simulations verified the effectiveness of the proposed method.

Keywords: NMV; enhanced triple power reaching law; sliding mode control; backstepping control; adaptive control; neural network control

check for updates

Citation: Huang, S.; Jiang, J.; Li, O. Adaptive Neural Network-Based Sliding Mode Backstepping Control for Near-Space Morphing Vehicle. *Aerospace* **2023**, *10*, 891. https://doi.org/10.3390/aerospace10100891

Academic Editor: Gokhan Inalhan

Received: 3 August 2023
Revised: 17 October 2023
Accepted: 17 October 2023
Published: 18 October 2023

1. Introduction

A near-space Morphing Vehicle (NMV) can cruise in the airspace from 20 to 100 km above the ground, and its cruising speed can exceed Mach 5 [1,2]. During cruise flight, NMV can conduct reconnaissance on ground and low airspace targets, monitor higher airspace targets, and complete tasks such as communication support. Therefore, cruise flight of NMV has always been a hot spot in aviation technology research [3–5]. However, NMV exhibits characteristics of high coupling, strong nonlinearity, and strong uncertainty [6], which bring difficulties to the flight control design of the NMV.

In the cruise phase, parameter uncertainty and a decrease in elevator control efficiency are exhibited in the NMV. Firstly, the inaccuracy of the model parameters of NMV is attributed to the difficulty in obtaining precise aerodynamic parameters. The high flight speed and altitude make it difficult to calculate the aerodynamic parameters of the aircraft accurately. Therefore, NMV has the problem of parameter uncertainty in the cruise phase. In addition, NMV in the cruising state is located in the near-space airspace, where atmospheric density is low and the air is thin, which leads to a reduction of the elevator control efficiency. At the same time, the cruising flight speed of the NMV is above Mach 5, and the dynamic pressure generated from flight is very large. With the increase in flying pressure, the elevator control efficiency of NMV continues to decline [7]. Therefore, the design of a cruise flight controller with strong robustness is particularly important to NMV.

In the nonlinear designs for near-space hypersonic vehicles, the backstepping control method can decompose the high-order nonlinear system into several low-order subsystems [8,9]. Therefore, the backstepping method can be employed for the design of the flight controller of a hypersonic vehicle [10–12]. For example, Zhang et al. proposed an anti-disturbance backstepping method based on ESO (extended state observer) to track and control the air-breathing hypersonic vehicle and achieved good tracking performance [13]. Based on the estimation of a double-layer fast adaptive-gain super-twisting disturbance observer, Zhang, X. et al. proposed a novel finite-time command-filtered backstepping scheme for flexible hypersonic vehicles [14]. However, backstepping control alone makes it difficult to achieve good robustness in the case of large parameter uncertainties. Sliding mode control can provide a solution to obtain better robustness in the presence of uncertainties [15–17]. However, the chattering phenomenon of sliding mode control is a disadvantage of sliding mode control; so, many sliding mode-based reaching laws have been proposed to reduce the chattering phenomenon, such as power sliding mode reaching law [18], double power reaching law [19], inverse hyperbolic reaching law [20], fast power reaching law [21], enhanced exponential reaching law [22], etc. However, these reaching laws still have room for improvement, and in order to reduce the negative effect of the chattering phenomenon and accelerate the convergence speed of the sliding mode system, better sliding mode reaching laws should be proposed. Adaptive control [23–25] can reduce the negative impact of parameter uncertainty on the system through the design of adaptive law. Therefore, adaptive robust control can be applied to NMV.

Neural networks [26,27] are a very effective method in the design of estimating unknown functions of a system. For example, Hao et al. proposed neural adaptive control schemes for air-breathing hypersonic vehicles. An adaptive RBFNN controller was developed to compensate for the saturation nonlinearity [28]. In Ref. [29], an adaptive neural network flight control system based on the backstepping method is proposed, and an RBF neural network is used to estimate the unknowns of the flight control system effectively. In order to reduce the adverse effects of system uncertainty, Xia et al. proposed the use of an RBF neural network to estimate the unknown nonlinearity of the speed and height of the subsystem, which enhanced the robustness of the system [30]. Therefore, the adaptive neural network can better approximate and compensate for the influence of unknown disturbances on NMV. However, due to the complexity of the nonlinear controller design of NMV, it is a great challenge to design a flight controller with good stability and robustness by fusing sliding mode control, backstepping control, and adaptive neural network together.

In the course of the cruise, the modes of NMV can be divided into level flight acceleration mode and altitude climbing mode according to different missions. In the flat flight acceleration mode, the flight altitude of NMV remains unchanged, and the flight speed increases. In the altitude climbing mode, NMV increases the flight altitude while maintaining the flight speed. In the level flight acceleration mode, the NMV retracts the winglets to reduce fuel consumption to reduce the adverse impact of flight drag. Whilst, in the altitude climbing mode, NMV stretches winglets to increase the aircraft's wing infiltration area, thereby increasing the lift coefficient. To sum up, in order to improve flight performance, NMV retracts winglets in flat flight acceleration mode, while stretching winglets in altitude climbing mode.

This paper merged the advantages of a neural network, sliding mode control, backstepping control, and adaptive control methods together to propose a sliding mode backstepping control method based on an adaptive neural network to guarantee stability and tracking accuracy of NMV in the cruise phase. The contributions of this paper are as follows:

(1) The changes in aerodynamic parameters of NMV in the states of winglets stretching and retracting were studied. It was found that NMV redrew winglets in the level flight mode of the cruise phase and stretched them in the altitude climbing mode, thus improving the flight efficiency of NMV in the cruise phase. (2) To ensure that the sliding mode control system can converge quickly and reduce chattering, an enhanced triple power reaching

law (ETPRL) was proposed. Then, in order to ensure stability and tracking performance of the control system, a sliding mode backstepping controller was designed. At the same time, an adaptive control law was designed to adaptively compensate negative effects of parameter uncertainty. (3) Aiming at the problem of reduction of elevator control efficiency, an adaptive neural network was used to estimate and compensate for interference in order to improve the robustness of the control system.

This paper is arranged as follows. Near-space morphing vehicle model is proposed and aerodynamic characteristic analysis is reported in Section 2. In Section 3, the design of a cruise controller based on the neural network sliding mode backstepping control is described. Then, stability analysis and proof are reported in Section 4. Simulation and verification of the NMV cruise flight controller based on neural network sliding mode backstepping control are reported in Section 5. Finally, a summary of key features of the proposed control scheme is shown in the final section.

2. Near-Space Morphing Vehicle Model and Aerodynamic Characteristics Analysis

The NMV studied in this paper adopts a wing-body fusion aerodynamic layout with variable winglets at the wing tip. The configuration of NMV is shown in Figure 1.

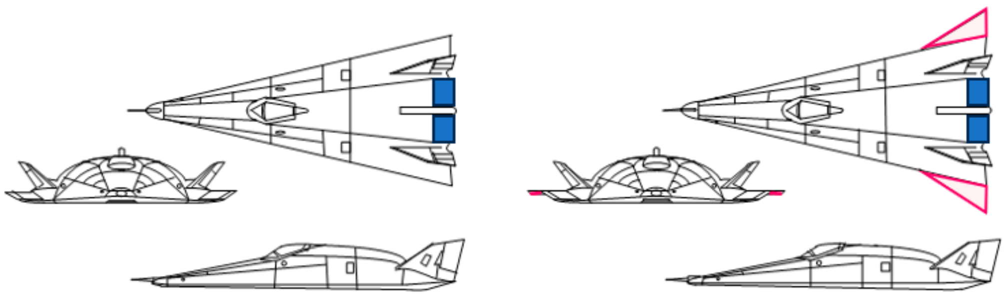

Figure 1. Diagram of NMV winglet contraction.

In Figure 1, winglets are highlighted in red, and elevators are highlighted in blue.

2.1. NMV Model Analysis

The longitudinal model of NMV is described by equations as follows [31,32]:

$$\begin{cases} \dot{V} = \frac{T\cos\alpha - D}{\mathrm{m}} - \frac{\mu}{r^2}\sin\gamma \\ \dot{\gamma} = \frac{L + T\sin\alpha}{mV} - \frac{\mu - V^2\mathrm{r}}{Vr^2}\cos\gamma \\ \dot{\alpha} = q - \dot{\gamma} \\ \dot{q} = \frac{M_{yy}}{I_{yy}} \\ \dot{h} = V\sin\gamma \\ \qquad \ddot{\beta} = -2\xi\omega\dot{\beta} - \omega^2\beta + \omega^2\beta_c \end{cases} \tag{1}$$

where the symbols with their descriptions are shown in Table 1 as follows:

Table 1. Model parameters of NMV.

Symbol	Description	Symbol	Description
V	Velocity, m/s	h	Altitude, m
γ	Flight path angle, rad	α	Attack angle, rad
q	Pitch angle rate, rad/s	β	State of the engine
m	Mass, kg	D	Drag
g	Acceleration of gravity, m/s^2	T	Thrust
μ	Earth's gravity constant	L	Lift
r	Radial distance from the Earth's center, m	M_{yy}	Pitch moment
I_{yy}	Rotation inertia, kg·m^2	ω	Natural frequency
ξ	Damp ratio	β_c	Throttle setting

The symbols M_{yy}, L, D, and T can be expressed as follows [31,32]:

$$\begin{cases} M_{yy} = \frac{1}{2}\rho V^2 s_w \bar{c}\left(C_M^\alpha + C_M^q + C_M^{\delta_e}\right) \\ L = \frac{1}{2}\rho V^2 s_w C_L \\ D = \frac{1}{2}\rho V^2 s_w C_D \\ T = \frac{1}{2}\rho V^2 s_w C_T \\ C_T = \begin{cases} 0.02576\beta & (\beta < 1) \\ 0.0224 + 0.00336\beta & (\beta \geq 1) \end{cases} \end{cases} \quad (2)$$

where ρ, s_w, $\bar{c}$, C_M^α, C_M^q, and $C_M^{\delta_e}$ are air density, wing area, mean aerodynamic chord, moment coefficient due to attack angle, moment coefficient due to pitch rate, and moment coefficient due to elevator deflection, respectively. C_L, C_D, and C_T are lift coefficient, drag coefficient, and engine thrust coefficient, respectively.

The linearized model of NMV is developed by repeatedly differentiating V three times and h four times as follows:

$$\begin{bmatrix} \dddot{V} & h^{(4)} \end{bmatrix}^T = \begin{bmatrix} \dddot{V}_0 & H_0^{(4)} \end{bmatrix}^T + \begin{bmatrix} b_{11} & b_{12} \\ b_{21} & b_{22} \end{bmatrix} \begin{bmatrix} \beta_c & \delta_e \end{bmatrix}^T \quad (3)$$

where

$$\begin{cases} \dddot{V}_0 & = \left(\dot{\boldsymbol{x}}^T \omega_2 \dot{\boldsymbol{x}} + \omega_1 \ddot{\boldsymbol{x}}_0\right)/m \\ H_0^{(4)} & = 3\ddot{V}\dot{\gamma}\cos\gamma - 3\dot{V}\dot{\gamma}^2\sin\gamma + 3\dot{V}\ddot{\gamma}\cos\gamma \\ & -3V\dot{\gamma}\ddot{\gamma}\sin\gamma - V\dot{\gamma}^3\cos\gamma + \left(\dot{\boldsymbol{x}}^T \omega_2 \dot{\boldsymbol{x}} + \omega_1 \ddot{\boldsymbol{x}}_0\right)\sin\gamma/m \\ & +V\cos\gamma\left(\pi_1 \ddot{\boldsymbol{x}}_0 + \dot{\boldsymbol{x}}^{\mathrm{T}} \pi_2 \dot{\boldsymbol{x}}\right) \\ b_{11} & = \left(\rho V^2 s c_\beta \omega^2/2m\right)\cos\alpha \\ b_{12} & = -\left(c_e \rho V^2 s \bar{c}/2m I_{yy}\right)\left(D_\alpha + T\sin\alpha\right) \\ b_{21} & = \left(\rho V^2 s c_\beta \omega^2/2m\right)\sin(\gamma + \alpha) \\ b_{22} & = \left(c_e \rho V^2 s \bar{c}/2m I_{yy}\right)\left[T\cos(\gamma+\alpha) + L_\alpha \cos\gamma - D_\alpha \sin\gamma\right] \end{cases} \quad (4)$$

In which, the detailed expression of the b_{11}, b_{12}, b_{21}, and b_{22} can be found in [32,33].

In the cruise phase, uncertainties are modeled as additive variance Δ to the nominal value, which is expressed as follows:

$$\begin{cases} m = m_0(1 + \Delta m) \\ I_{yy} = I_{yy0}(1 + \Delta I_{yy}) \\ \rho = \rho_0(1 + \Delta\rho) \\ s_w = s_{w0}(1 + \Delta s_w) \\ \bar{c} = \bar{c}_0(1 + \Delta\bar{c}) \\ c_e = c_{e0}(1 + \Delta c_e) \\ C_L = C_{L0}(1 + \Delta C_L) \\ C_D = C_{D0}(1 + \Delta C_D) \\ C_T = C_{T0}(1 + \Delta C_T) \\ C_M^\alpha = C_{M0}^\alpha(1 + \Delta C_M^\alpha) \\ C_M^q = C_{M0}^q\left(1 + \Delta C_M^q\right) \\ C_M^{\delta_e} = C_{M0}^{\delta_e}\left(1 + \Delta C_M^{\delta_e}\right) \end{cases} \quad (5)$$

2.2. Analysis of NMV Winglet Deformation

In order to better analyze the influence of winglet deformation on NMV, the influence of winglet state on aerodynamic characteristics is first studied in this section.

When the NMV is in the retracting state, the reference area and the reference length of the wing are: $s_w = 369\ \mathrm{m}^2$ and $\bar{c} = 27$ m, respectively; and $\mathrm{s_w} = 389\ \mathrm{m}^2$, $\bar{c} = 30$ m, respectively, when the NMV's winglets are in the stretching state.

2.2.1. Lift of Different Winglet Deformation States

The lift of the aircraft is mainly generated by the wing, of which the size is mainly determined by the infiltration area of the wing, atmospheric density, flight speed, and lift coefficient.

As shown in Figure 1, retractable winglets are designed to be located at the NMV wing tip, so parameters of the aircraft wing can vary with the change of winglets, which has an important impact on lift.

The lift expression of NMV with winglets retracted is expressed as follows:

$$L = f(Ma, \alpha, \delta_e) = \left(0.5\rho V^2\right) s_w C_L = \left(0.5\rho V^2\right) s_w \left(C_{L0} + C_{L\alpha}\alpha + C_{L\delta_e}\delta_e\right) \tag{6}$$

The lift expression of NMV with winglets stretched is as follows:

$$L = f(Ma, \alpha, \delta_e, \delta_v) = \left(0.5\rho V^2\right)(s_w + \Delta S_w)\left(C_{L0} + C_{L\alpha}\alpha + C_{L\delta_e}\delta_e + C_{L\delta_v}\delta_v\right) \tag{7}$$

where δ_v, ΔS_w, and $C_{L\delta_v}$ represent the variation of winglet contraction, the variation of wing infiltrated area caused by winglet contraction, and the change in coefficient of lift caused by winglet contraction, respectively. In order to compare the effects of stretching and retracting winglets on lift, Figure 2 shows a three-dimensional surface among lift coefficient, flight Mach number, and flight angle of attack under the states of winglet stretching and winglet retracting.

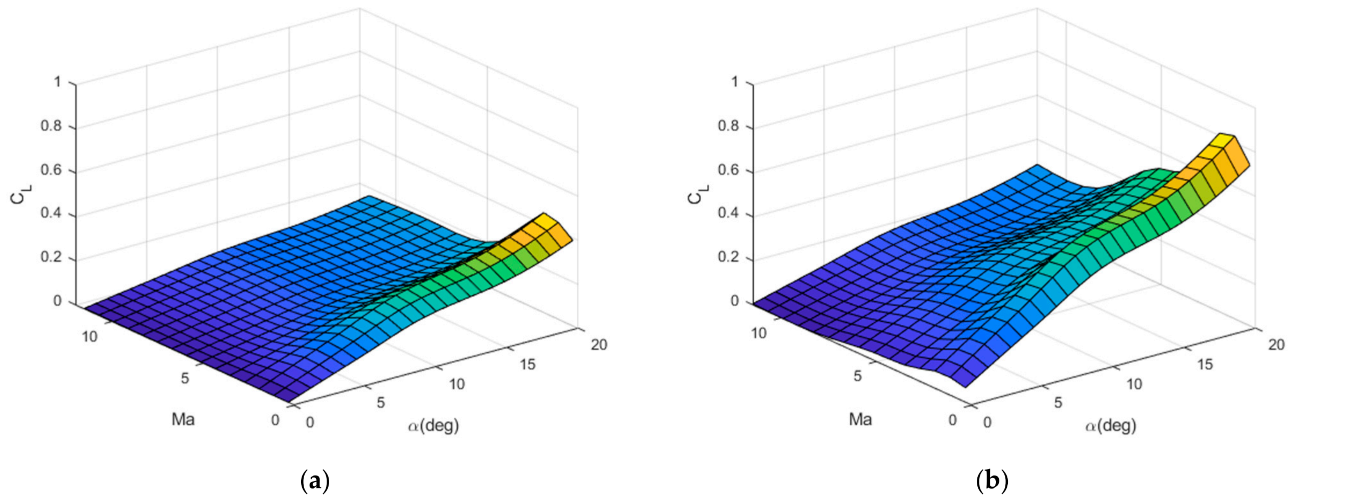

Figure 2. Lift coefficients of NMV winglets in retracting and stretching state. (**a**) Winglet retracting. (**b**) Winglet stretching.

2.2.2. Drag of Different Winglet States

The flight drag of the NMV with winglets retracted is expressed as follows:

$$D = \left(0.5\rho V^2\right) s_w \left(C_{D0} + C_{D\alpha}\alpha + C_{D\delta_e}\delta_e\right) \tag{8}$$

The flight drag of NMV with winglets stretched is expressed as follows:

$$D = \left(0.5\rho V^2\right)(s_w + \Delta S_w)\left(C_{D0} + C_{D\alpha}\alpha + C_{D\delta_e}\delta_e + C_{D\delta_v}\delta_v\right) \tag{9}$$

where $C_{D\delta_v}$ represents the drag change coefficient caused by winglet contraction. In order to compare the effects of winglet stretching and retracting on flight drag, and the relation among drag coefficient, flight Mach number, and angle of attack, the changes in the curve of the drag coefficient under the states of winglet stretching and retracting can be drawn, respectively, as shown in Figure 3.

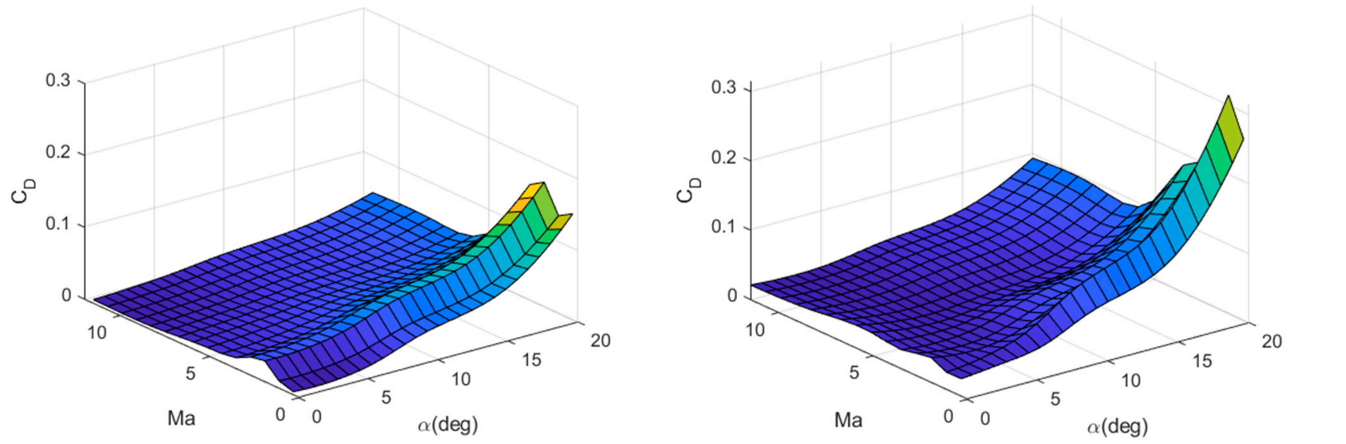

(**a**) (**b**)

Figure 3. Drag coefficients of NMV winglets in retracting and stretching state. (**a**) Winglet retracting. (**b**) Winglet stretching.

2.2.3. Pitching Moment of Different Winglet States

The pitching moment of the NMV with winglets retracted is expressed as follows:

$$M_A = \left(0.5\rho V^2\right)s_w c_A\left(C_{m0} + C_{m\alpha}\beta + C_{m\delta_e}\delta_e + C_{m\bar{q}}\bar{q} + C_{m\dot{\bar{\alpha}}}\dot{\bar{\alpha}} + C_{m\dot{\bar{\delta}}_e}\dot{\bar{\delta}}_e\right) \tag{10}$$

The pitching moment of NMV with winglets stretched is expressed as follows:

$$\begin{aligned} M_A \quad &= (0.5\rho V^2)(s_w + \Delta S_w)(c_A + \Delta c_A)(C_{m0} + C_{m\alpha}\beta + C_{m\delta_e}\delta_e + C_{m\bar{q}}\bar{q} \\ &+C_{m\dot{\bar{\alpha}}}\dot{\bar{\alpha}} + C_{m\dot{\bar{\delta}}_e}\dot{\bar{\delta}}_e + C_{m\delta_v}\delta_v) \end{aligned} \tag{11}$$

where $C_{m\delta_v}$ and Δc_A represent the variation coefficient of pitching moment and variation of average aerodynamic chord length caused by winglet contraction, respectively. When the winglet state is switched, the wing area, the mean aerodynamic chord, and the pitch moment coefficient of the aircraft will change. In order to compare the effects of winglet stretching and retracting on the pitch moment coefficient of flight and the relationship among pitch moment coefficient, flight Mach number, and angle of attack, the changes in the curve of pitch moment coefficient under winglet stretching or retracting can be drawn, respectively, as shown in Figure 4.

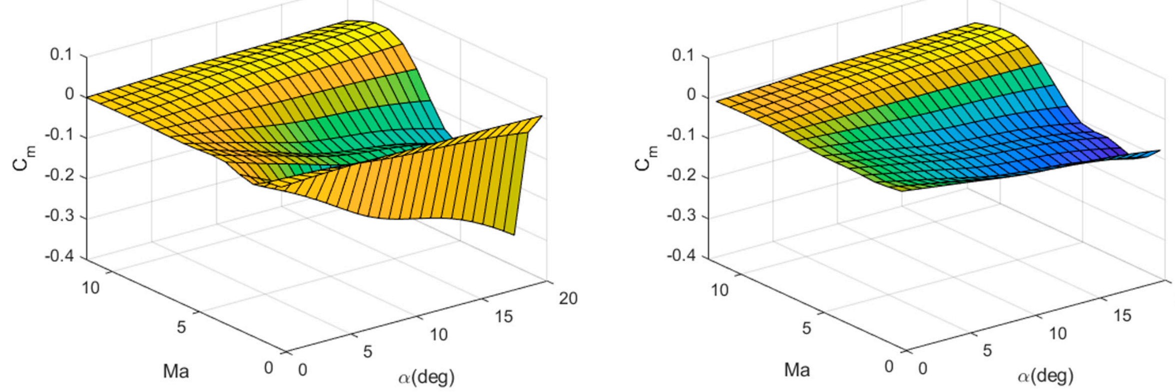

(**a**) (**b**)

Figure 4. Pitch moment coefficients of NMV winglets in retracting and stretching state. (**a**) Winglet retracting. (**b**) Winglet stretching.

To sum up, the NMV can change the shape of the aircraft through expansion and contraction of the winglets, resulting in changes in the wing area, average aerodynamic chord length, and various aerodynamic parameters of the aircraft, so as to change the lift, drag, and pitching moment of the aircraft. Through the change of winglets, the aircraft can obtain better aerodynamic performance and better adaptation to the needs of different flight tasks.

NMV can stretch and retract the winglets according to the changes in the flight environment or mission requirements. When NMV needs to quickly raise the flight altitude, it can stretch the winglets to improve the lift. Whereas, when the NMV does not need to raise the altitude, winglets can be retracted to reduce flight drag, improve flight efficiency, and obtain good flight performance of the NMV. Therefore, in the level flight acceleration mode, in order to reduce the drag, the NMV retracts the winglets; while in the altitude climbing mode, the NMV stretches the winglets to increase lift.

3. Design of Cruise Controller Based on an Adaptive Neural Network Sliding Mode Backstepping Control

3.1. System Structure Frame Diagram

Aiming at the issues of decreasing elevator control efficiency and uncertainty in the cruising phase of the NMV, a sliding mode backstepping control method based on a neural network is proposed in this paper. The proposed control system structure is shown in Figure 5.

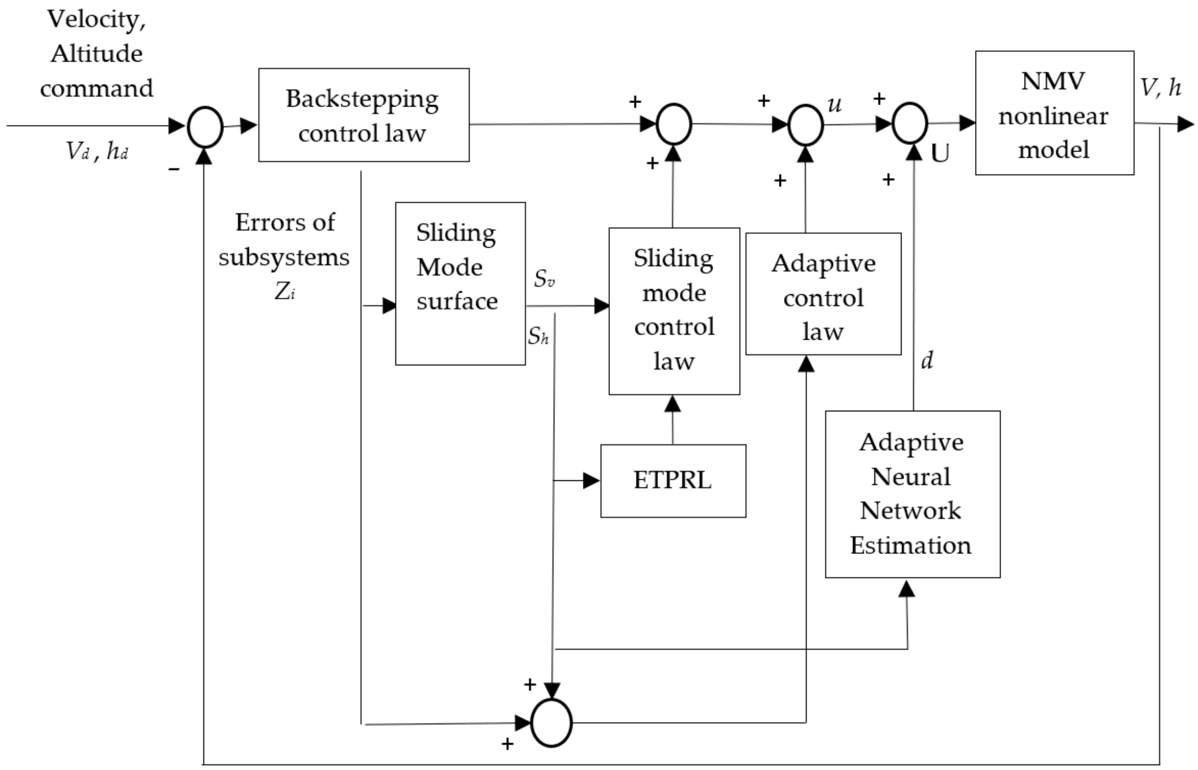

Figure 5. System structure of sliding mode backstepping controller based on an adaptive neural network.

In Figure 5, the virtual control law and subsystem error Zi (i = 1, 2, 3, 4) of four low-order subsystems are obtained by the backstepping control method after four backward recursions. In the last step of backstepping design, sliding mode control is integrated to improve the robustness of the system. In order to ensure rapid convergence of the sliding mode control system under the condition of reducing elevator control efficiency, an enhanced triple power reaching law (ETPRL) is proposed. At the same time, in order to estimate and compensate for the uncertainty of each subsystem adaptively, adaptive control laws are designed. In addition, the RBF neural network is used to estimate and compensate for control channel interference so as to improve the tracking accuracy and robustness of the system.

3.2. Design of an Enhanced Triple Power Reaching Law

In order to accelerate the convergence rate of sliding mode systems and reduce chattering, this paper proposes an enhanced triple power reaching law (ETPRL), which is expressed as follows:

$$\dot{s} = -l_1|s|^{\alpha_s}sgn(s) - l_2|s|^{\beta_s}sgn(s) - l_3|s|^{\gamma_s}sgn(s) - l_4 s \tag{12}$$

where s is a sliding mode surface; $sgn(s)$ is a signum function: $l_1 > 0$, $l_2 > 0$, $l_3 > 0$, $l_4 > 0$, $\alpha_s > 1$, and $0 < \beta_s < 1$; and γ_s is a variable parameter.

$$\gamma_s = \begin{cases} \delta, & |s| > \omega_s \\ 1, & |s| \le \omega_s \end{cases} \tag{13}$$

where δ and ω_s are set constants, and $\delta > \alpha_s$ and $\omega_s > 1$.

Theorem 1. *For the reaching law of sliding mode control given as Equation (12), the state of system s converges to the equilibrium point in fixed time.*

Proof of Theorem 1.

1. Analysis of accessibility

According to Equation (12), we obtain the following:

$$\begin{aligned} s\dot{s} &= s\left[-l_1|s|^{\alpha_s}sgn(s) - l_2|s|^{\beta_s}sgn(s) - l_3|s|^{\gamma_s}sgn(s) - l_4 s\right] \\ &= -l_1|s|^{\alpha_s+1} - l_2|s|^{\beta_s+1} - l_3|s|^{\gamma_s+1} - l_4 s^2 \le 0 \end{aligned} \tag{14}$$

If and only if $s = 0$, $s\dot{s} = 0$ can be attained. When s $\neq 0$, according to the reaching law $\dot{s} \neq 0$, the reaching law $\dot{s}$ causes the sliding mode surface function s to vary instead of being a fixed constant. Gradually, s will approach 0 until $s\dot{s} = 0$ when s $= 0$.

Based on the above analysis, the system state s can reach the equilibrium point $s = 0$.

2. Analysis of fixed-time convergence

We assume that the initial state of the system is defined as $|s_0| > \omega > 1$. Then, the convergence process of the system can be divided into three stages: $s_0 \to s(t_1) = \omega \to s(t_2) = 1 \to s(t_3) = 0$. For the convenience of analysis, we assume that the parameters of Equation (12) are set as follows: $l_1 = l_2 = l_3 = l_4$.

(1) $s_0 \to s(t_1) = \omega_s$

In the first stage, $\gamma_s = \delta, \delta > \alpha_s > \beta_s$, and then, $|s|^{\gamma} > |s|^{\alpha_s} > |s|^{\beta_s}$. Compared with the first and second terms in Equation (12), the third term $-l_3|s|^{\gamma_s}sgn(s)$ plays a major role in the reaching law. Therefore, Equation (12) can be expressed as follows:

$$\dot{s} = -l_3|s|^{\gamma_s}sgn(s) - l_4 s \tag{15}$$

Integrating Equation (15), we obtain the following:

$$s^{1-\gamma_s} = \left(s_0{}^{1-\gamma_s} + \frac{l_3}{l_4}\right)e^{-(1-\gamma_s)l_4 t} - \frac{l_3}{l_4} \tag{16}$$

Then, the convergence time of this stage can be expressed as follows:

$$t_1 = \frac{1}{(1-\gamma_s)l_4}\left[ln\left({\gamma_s}^{1-\gamma_s} + \frac{l_3}{l_4}\right) - ln\left({s_0}^{1-\gamma_s} + \frac{l_3}{l_4}\right)\right] \tag{17}$$

At this stage, for the convenience of calculation, t_1 in Equation (17) is used as the approach time of the system considering only the third and fourth terms of Equation (12). The other two items of Equation (12) can also speed up the convergence time of the system state, although the effect is not obvious. Thus, the time required for the system to go from s_0 to $s(t_1)$ is less than t_1.

(2) $s(t_1) = \omega_s \to s(t_2) = 1$

In the second stage, $\gamma_s = 1$, $\alpha_s > \gamma_s > \beta_s > 0$, and then $|s|^{\alpha_s} > |s|^{\gamma_s} > |s|^{\beta_s}$. Thus, compared with second and third in Equation (12), the first term $-l_1|s|^{\alpha}sgn(s)$ plays a major role in the reaching law. Therefore, Equation (12) can be expressed as follows:

$$\dot{s} = -l_1|s|^{\alpha_s}sgn(s) - l_4 s \tag{18}$$

Integrating Equation (18), we obtain the following:

$$s^{1-\alpha_s} = (1 + \frac{l_1}{l_4})e^{-(1-\alpha_s)l_4 t} - \frac{l_1}{l_4} \tag{19}$$

Then, the max reaching time in this stage can be expressed as follows:

$$t_2 = \frac{1}{(1-\alpha_s)l_4}\left[ln\left(1 + \frac{l_1}{l_4}\right) - ln\left({\omega_s}^{1-\alpha_s} + \frac{l_1}{l_4}\right)\right] \tag{20}$$

Therefore, the same analysis as in step (1), the time required for the system to go from $s(t_1)$ to $s(t_2)$ is less than t_2.

(3) $s(t_2) = 1 \to s(t_3) = 0$

In this stage, s < 1, $|s|^{\beta_s} > |s|^{\gamma_s} > |s|^{\alpha_s}$. Compared with the first and third terms in Equation (12), the second term $-l_2|s|^{\beta_s}sgn(s)$ plays a major role in the reaching law. Therefore, Equation (12) can be expressed as follows:

$$\dot{s} = -l_2|s|^{\beta_s}sgn(s) - l_4 s \tag{21}$$

Integrating Equation (21), we have:

$$s^{1-\beta_s} = \left(1 + \frac{l_2}{l_4}\right)e^{-(1-\beta_s)l_4 t} - \frac{l_2}{l_4} \tag{22}$$

Then, the convergence time of this stage can be calculated from the above formula:

$$t_3 = \frac{1}{(\beta_s - 1)l_4}\left[ln\left(s^{1-\beta_s} + \frac{l_2}{l_4}\right) - ln\left(1 + \frac{l_2}{l_4}\right)\right] \tag{23}$$

In the same way, the time required for the system to go from $s(t_2)$ to $s(t_3)$ is less than t_3.
When Equations (17), (20), and (23) can be seen, t_1, t_2, and t_3 can be reduced by setting $l_4 > 0$, which can obtain a faster convergence speed.
Above all, for the reaching law ETPRL, the reaching time T satisfies the following formula:

$$T < t_1 + t_2 + t_3 \tag{24}$$

The proof is completed. □

3.3. Sliding Mode Backstepping Control Design Based on Neural Network

According to the NMV input–output feedback linearization model of Equation (3), the NMV feedback linearization model can be expressed as the following nonlinear system:

$$\begin{cases} \dot{x}_1 = x_2 + \varphi_1^T(x_1)\theta_1 \\ \dot{x}_2 = x_3 + \varphi_2^T(x_2)\theta_2 \\ \dot{x}_3 = x_4 + \varphi_3^T(x_3)\theta_3 \\ \dot{x}_4 = f(x,t) + G(x,t)(u+d) + \varphi_4^T(x_4)\theta_4 \end{cases} \tag{25}$$

of which,

$$\begin{cases} f(x,t) = \begin{bmatrix} f_V & f_h \end{bmatrix}^T \\ G(x,t) = \begin{bmatrix} b_{11} & b_{12} \\ b_{21} & b_{22} \end{bmatrix} \\ u = \begin{bmatrix} \beta_c & \delta_e \end{bmatrix}^T \end{cases} \tag{26}$$

where $x_i = \begin{bmatrix} x_{i,1}, & x_{i,2} \end{bmatrix}^T \in R^2 (i = 1,2,3,4)$ are system state variables—among them, $x_1 = \begin{bmatrix} \int_0^{\mathrm{t}} (\mathrm{V}(\tau)\, d\tau & \mathrm{h} \end{bmatrix}^{\mathrm{T}}, x_2 = \begin{bmatrix} V & \dot{h} \end{bmatrix}^T, x_3 = \begin{bmatrix} \dot{V} & \ddot{h} \end{bmatrix}^T, x_4 = \begin{bmatrix} \ddot{V} & \dddot{h} \end{bmatrix}^T$; $f(x,t)$ and $G(x,t)$ are known nonlinear functions; $u \in R^2$ is control input; $\varphi_i^T(x_i)\theta_i,\ i = 1,2,3,4$ represents the uncertainty of each subsystem; $\varphi_i^T(x_i) = diag\begin{bmatrix} \varphi_{i,1}, \varphi_{i,2} \end{bmatrix}$ are known functions, which are assumed to be sufficiently smooth; d indicates interference on the control channel; and $\theta_i = \begin{bmatrix} \theta_{i,1}, \theta_{i,2} \end{bmatrix}^T$ are unknown constant parameters, where θ_i is defined as follows:

$$\theta_i = \hat{\theta}_i + \widetilde{\theta}_i \tag{27}$$

where $\hat{\theta}_i$ is the estimation of θ_i, $\widetilde{\theta}_i$ is an estimation error. The interference on the NMV control channel is defined as follows:

$$d = \hat{d} + \widetilde{d} \tag{28}$$

where $d = \begin{bmatrix} d_{\beta_c}, & d_{\delta_e} \end{bmatrix}^T$ represents the amount of interference on the NMV actuator.

In this paper, the RBF neural network is used to approximate d, where $\hat{d}$ is the estimate of the RBF neural network and $\widetilde{d}$ is an approximation error.

The sliding mode backstepping controller design steps are as follows:

According to Equation (25), the system is divided into four low-order subsystems, and the error of each low-order subsystem is defined as follows:

$$\begin{cases} z_1 = x_1 - \mu_1 \\ z_2 = x_2 - \mu_2 \\ z_3 = x_3 - \mu_3 \\ z_4 = x_4 - \mu_4 \end{cases} \tag{29}$$

where $\mu_1 = x_{1\mathrm{d}} = \begin{bmatrix} \int_0^{\mathrm{t}} \mathrm{V_d}(\tau)\mathrm{d}\tau & \mathrm{h_d} \end{bmatrix}^{\mathrm{T}}$ represents the instruction signal of the first subsystem, $\mathrm{V_d}$ and $\mathrm{h_d}$ are the desired commanded values of velocity and altitude, respectively; μ_2, μ_3, and μ_4 are the virtual control quantities of the second, the third, and the fourth subsystems, respectively. The virtual control quantity is designed as follows:

$$\begin{cases} \mu_2 = -k_1 z_1 + \dot{\mu}_1 - \varphi_1^T(x_1)\hat{\theta}_1 \\ \mu_3 = -k_2 z_2 + \dot{\mu}_2 - z_1 - \varphi_2^T(x_2)\hat{\theta}_2 \\ \mu_4 = -k_3 z_3 + \dot{\mu}_3 - z_2 - \varphi_3^T(x_3)\hat{\theta}_3 \end{cases} \tag{30}$$

Step 1:

Considering the first subsystem $\dot{x}_1 = x_2 + \varphi_1^T(x_1)\theta_1$ of Equation (25), we obtain the following after the tracing error expression $z_1 = x_1 - \mu_1$ is differentiated:

$$\dot{z}_1 = \dot{x}_1 - \dot{\mu}_1 = x_2 + \varphi_1^T(x_1)\theta_1 - \dot{\mu}_1 \tag{31}$$

In order to stabilize the first subsystem, the virtual control law μ_2 is defined as follows:

$$\mu_2 = -k_1 z_1 + \dot{\mu}_1 - \varphi_1^T(x_1)\hat{\theta}_1 \tag{32}$$

where $k_1 > 0$.

According to Equation (29), the tracking error of the second subsystem is as follows:

$$z_2 = x_2 - \mu_2 \tag{33}$$

Substituting Equation (32) into Equation (33), we obtain the following:

$$x_2 = -k_1 z_1 + \dot{\mu}_1 + z_2 - \varphi_1^T(x_1)\hat{\theta}_1 \tag{34}$$

Substituting Equation (34) into Equation (31), we obtain the following:

$$\begin{aligned} \dot{z}_1 &= -k_1 z_1 + z_2 + \varphi_1^T(x_1)\theta_1 - \varphi_1^T(x_1)\hat{\theta}_1 \\ &= -k_1 z_1 + z_2 + \varphi_1^T(x_1)\widetilde{\theta}_1 \end{aligned} \tag{35}$$

The Lyapunov function of the first subsystem is selected as follows:

$$V_1 = \frac{1}{2} z_1^T z_1 + \frac{1}{2}\widetilde{\theta}_1^T \Gamma_1^{-1} \widetilde{\theta}_1 \tag{36}$$

where Γ_1 is a symmetric positive definite matrix. And $\Gamma_i,\ i = 2{,}3{,}4$ in the later steps were also set to symmetric positive definite matrices.

Taking the derivative of Equation (36) and substituting Equation (35), we obtain the following:

$$\begin{aligned} \dot{V}_1 &= z_1^T\left(-k_1 z_1 + z_2 + \varphi_1^T(x_1)\widetilde{\theta}_1\right) + \widetilde{\theta}_1^T \Gamma_1^{-1}\left(\dot{\theta}_1 - \dot{\hat{\theta}}_1\right) \\ &= -k_1 z_1^T z_1 + z_1^T z_2 + z_1^T \varphi_1^T(x_1)\widetilde{\theta}_1 + \widetilde{\theta}_1^T \Gamma_1^{-1}\left(\dot{\theta}_1 - \dot{\hat{\theta}}_1\right) \\ &= -k_1 z_1^T z_1 + z_1^T z_2 + \widetilde{\theta}_1^T\left(\varphi_1(x_1) z_1 - \Gamma_1^{-1}\dot{\hat{\theta}}_1\right) \end{aligned} \tag{37}$$

Step 2:

For the second subsystem $\dot{x}_2 = x_3 + \varphi_2^T(x_2)\theta_2$ of Equation (25), we obtain the following after the tracing error expression $z_2 = x_2 - \mu_2$ is differentiated:

$$\begin{aligned} \dot{z}_2 &= -k_2 z_2 - z_1 + z_3 + \varphi_2^T(x_2)\theta_2 - \varphi_2^T(x_2)\hat{\theta}_2 \\ &= -k_2 z_2 - z_1 + z_3 + -\varphi_2^T(x_2)\widetilde{\theta}_2 \end{aligned} \tag{38}$$

The Lyapunov function of the second subsystem is defined as follows:

$$V_2 = V_1 + \frac{1}{2} z_2^T z_2 + \frac{1}{2}\widetilde{\theta}_2^T \Gamma_2^{-1} \widetilde{\theta}_2 \tag{39}$$

Taking the derivative of Equation (39), we obtain the following:

$$\begin{aligned}\dot{V}_2 &= \dot{V}_1 + z_2^T\left(-k_2z_2 - z_1 + z_3 + \varphi_2^T(x_2)\tilde{\theta}_2\right) + \tilde{\theta}_2^T\Gamma_2^{-1}\left(\dot{\theta}_2 - \dot{\hat{\theta}}_2\right) \\ &= \dot{V}_1 + z_2^T(-k_2z_2 - z_1 + z_3) + z_2^T\varphi_2^T(x_2)\tilde{\theta}_2 + \tilde{\theta}_2^T\Gamma_2^{-1}\left(\dot{\theta}_2 - \dot{\hat{\theta}}_2\right) \\ &= -k_1z_1^Tz_1 - k_2z_2^Tz_2 + z_2^Tz_3 + \tilde{\theta}_1^T\left(\varphi_1(x_1)z_1 - \Gamma_1^{-1}\dot{\hat{\theta}}_1\right) + \tilde{\theta}_2^T\left(\varphi_2(x_2)z_2 - \Gamma_2^{-1}\dot{\hat{\theta}}_2\right) \\ &= \sum_{i=1}^{2}[-k_iz_i^Tz_i + \tilde{\theta}_i^T\left(\varphi_i(x_i)z_i - \Gamma_i^{-1}\dot{\hat{\theta}}_i\right)] + z_2^Tz_3\end{aligned} \tag{40}$$

Step 3:

Similarly, for the third subsystem $\dot{x}_3 = x_4 + \varphi_3^T(x_3)\theta_3$ of Equation (25), after the tracing error expression $z_3 = x_3 - \mu_3$ is differentiated, we obtain the following:

$$\dot{z}_3 = \dot{x}_3 - \dot{\alpha}_3 = x_4 + \varphi_3^T(x_3)\theta_3 - \dot{\mu}_3 \tag{41}$$

According to Equation (29), the tracking error of the fourth subsystem is as follows:

$$z_4 = x_4 - \mu_4 \tag{42}$$

In order to ensure the stability of the subsystem, the virtual control input is defined as follows:

$$\mu_4 = -k_3z_3 + \dot{\mu}_3 - z_2 - \varphi_3^T(x_3)\hat{\theta}_3 \tag{43}$$

where $k_3 > 0$. Substituting Equations (42) and (43) into Equation (41), we obtain the following:

$$\begin{aligned}\dot{z}_3 &= -k_3z_3 - z_2 + z_4 + \varphi_3^T(x_3)\theta_3 - \varphi_3^T(x_3)\hat{\theta}_3 \\ &= -k_3z_3 - z_3 + z_4 + \varphi_3^T(x_3)\tilde{\theta}_3\end{aligned} \tag{44}$$

The Lyapunov function of the third subsystem is defined as follows:

$$V_3 = V_2 + \frac{1}{2}z_3^Tz_3 + \frac{1}{2}\tilde{\theta}_3^T\Gamma_3^{-1}\tilde{\theta}_3 \tag{45}$$

Take the derivative of Equation (45), we obtain the following:

$$\begin{aligned}\dot{V}_3 &= \dot{V}_2 + z_3^T(-k_3z_3 - z_3 + z_3) + \tilde{\theta}_3^T(z_3 - \Gamma_3^{-1}\dot{\hat{\theta}}_3) \\ &= -k_1z_1^Tz_1 - k_2z_2^Tz_2 - k_3z_3^Tz_3 + z_3^Tz_4 + \tilde{\theta}_1^T\left(\varphi_1(x_1)z_1 - \Gamma_1^{-1}\dot{\hat{\theta}}_1\right) \\ &+ \tilde{\theta}_2^T\left(\varphi_2(x_2)z_2 - \Gamma_2^{-1}\dot{\hat{\theta}}_2\right) + \tilde{\theta}_3^T(\varphi_3(x_3)z_3 - \Gamma_3^{-1}\dot{\hat{\theta}}_3) \\ &= \sum_{i=1}^{3}[-k_iz_i^Tz_i + \tilde{\theta}_i^T(\varphi_i(x_i)z_i - \Gamma_i^{-1}\dot{\hat{\theta}}_i)] + z_3^Tz_4\end{aligned} \tag{46}$$

Step 4:

The design of the sliding mode surface is as follows:

$$S = \begin{bmatrix} s_V \\ s_h \end{bmatrix} = c_1z_1 + c_2z_2 + c_3z_3 + z_4 \tag{47}$$

where $S \in R^2$, $c_i > 0$, $i = 1,2,3$. By differentiating Equation (47), we obtain the following:

$$\begin{aligned}\dot{S} &= c_1\dot{z}_1 + c_2\dot{z}_2 + c_3\dot{z}_3 + \dot{z}_4 \\ &= c_1\dot{z}_1 + c_2\dot{z}_2 + c_3\dot{z}_3 + \dot{x}_4 - \dot{\mu}_4\end{aligned} \tag{48}$$

Substituting the expression $\dot{x}_4 = f(x,t) + G(x,t)[u+d] + \varphi_4^T(x_4)\theta_4$ of the fourth subsystem of Equation (25) into Equation (48), we obtain the following:

$$\dot{S} = c_1\dot{z}_1 + c_2\dot{z}_2 + c_3\dot{z}_3 + f(x,t) + G(x,t)[u+d] + \varphi_4^T(x_4)\theta_4 - \dot{\mu}_4 \tag{49}$$

The Lyapunov function of the fourth subsystem is defined as follows:

$$V_4 = V_3 + \frac{1}{2}S^T S + \frac{1}{2}\tilde{\theta}_4^T \Gamma_4^{-1}\tilde{\theta}_4 = \frac{1}{2}\sum_{i=1}^{3} k_i z_i^T z_i + \frac{1}{2}S^T S + \frac{1}{2}\sum_{j=1}^{4}\tilde{\theta}_j^T \Gamma_j^{-1}\tilde{\theta}_j \tag{50}$$

Taking the derivative of Equation (50) and substituting Equation (46) into the result, we obtain the following:

$$\begin{aligned}
\dot{V}_4 &= \dot{V}_3 + S^T\dot{S} + \tilde{\theta}_4^T\Gamma_4^{-1}\dot{\tilde{\theta}}_4 \\
&= \dot{V}_3 + S^T\left[\sum_{i=1}^{3} c_i\dot{z}_i + f(x,t) + G(x,t)u + \varphi_4^T(x_4)\theta_4 - \dot{\mu}_4\right] + \tilde{\theta}_4^T\Gamma_4^{-1}\left(\dot{\theta}_4 - \dot{\hat{\theta}}_4\right) \\
&= \sum_{i=1}^{3}[-k_i z_i^T z_i + \tilde{\theta}_i^T(\varphi_i(x_i)z_i - \Gamma_i^{-1}\dot{\hat{\theta}}_i)] + z_3^T z_4 + S^T[\sum_{i=1}^{3} c_i\dot{z}_i + f(x,t) \\
&\quad + G(x,t)[u+d] + \varphi_4^T(x_4)\hat{\theta}_4 - \dot{\mu}_4] + \tilde{\theta}_4^T[\varphi_4(x_4)S - \Gamma_4^{-1}\dot{\hat{\theta}}_4]
\end{aligned} \tag{51}$$

By substituting Equation (47) into Equation (51), we obtain the following:

$$\begin{aligned}
\dot{V}_4 = &\sum_{i=1}^{3}[-k_i z_i^T z_i + \tilde{\theta}_i^T(\varphi_i(x_i)z_i - \Gamma_i^{-1}\dot{\hat{\theta}}_i)] + z_3^T\left(S - \sum_{i=1}^{3} c_i z_i\right) \\
&+ S^T\left[\sum_{i=1}^{3} c_i\dot{z}_i + f(x,t) + G(x,t)[u+d] + \varphi_4^T(x_4)\hat{\theta}_4 - \dot{\mu}_4\right] \\
&+ \tilde{\theta}_4^T\left[\varphi_4(x_4)S - \Gamma_4^{-1}\dot{\hat{\theta}}_4\right] \\
= &\sum_{i=1}^{3}[-k_i z_i^T z_i + \tilde{\theta}_i^T(\varphi_i(x_i)z_i - \Gamma_i^{-1}\dot{\hat{\theta}}_i)] + z_3^T\sum_{i=1}^{3} c_i z_i \\
&+ S^T\left[z_3 + \sum_{i=1}^{3} c_i\dot{z}_i + f(x,t) + G(x,t)[u+d] + \varphi_4^T(x_4)\hat{\theta}_4 - \dot{\mu}_4\right] \\
&+ \tilde{\theta}_4^T\left[\varphi_4(x_4)S - \Gamma_4^{-1}\dot{\hat{\theta}}_4\right]
\end{aligned} \tag{52}$$

After further collating Equation (52), we can obtain the following:

$$\begin{aligned}
\dot{V}_4 = &-\sum_{i=1}^{3} k_i z_i^T z_i - z_3^T\sum_{i=1}^{3} c_i z_i + S^T[z_3 + \sum_{i=1}^{3} c_i\dot{z}_i + f(x,t) + G(x,t)[u+d] \\
&+ \varphi_4^T(x_4)\hat{\theta}_4 - \dot{\mu}_4] + \sum_{i=1}^{3}\tilde{\theta}_i^T[\varphi_i(x_i)z_i - \Gamma_i^{-1}\dot{\hat{\theta}}_i] + \tilde{\theta}_4^T[\varphi_4(x_4)S - \Gamma_4^{-1}\dot{\hat{\theta}}_4] \\
= &-z^T Q z + S^T[z_3 + \sum_{i=1}^{3} c_i\dot{z}_i + f(x,t) + G(x,t)[u+d] \\
&+ \varphi_4^T(x_4)\hat{\theta}_4 - \dot{\mu}_4] + \sum_{i=1}^{3}\tilde{\theta}_i^T[\varphi_i(x_i)z_i - \Gamma_i^{-1}\dot{\hat{\theta}}_i] + \tilde{\theta}_4^T[\varphi_4(x_4)S - \Gamma_4^{-1}\dot{\hat{\theta}}_4]
\end{aligned} \tag{53}$$

where

$$\left\{\begin{aligned}
z &= \begin{bmatrix} z_1 & z_2 & z_3 \end{bmatrix}^T \\
Q &= \begin{bmatrix} k_1 & 0 & 0 \\ 0 & k_2 & 0 \\ c_1 & c_2 & k_3 + c_3 \end{bmatrix}
\end{aligned}\right. \tag{54}$$

According to the controller design process, Q is a positive definite matrix.

To ensure the stability of the control system, the controller is designed as follows:

$$u = G(x,t)^{-1}\left(-z_3 - \sum_{i=1}^{3} c_i \dot{z}_i - f(x,t) - \varphi_4^T(x_4)\hat{\theta}_4 + \dot{\mu}_4 + u_{sw}\right) - d \tag{55}$$

where $u_{sw} \in R^2$, which uses the enhanced triple power reaching law ETPRL. u_{sw} is designed as follows:

$$u_{sw} = \begin{bmatrix} -l_{1,1}|s_1|^{\alpha_{s1}} sgn(s_1) - l_{1,2}|s_1|^{\beta_{s1}} sgn(s_1) - l_{1,3}|s_1|^{\gamma_{s1}} sgn(s_1) - l_{1,4}s_1 \\ -l_{2,1}|s_2|^{\alpha_{s2}} sgn(s_2) - l_{2,2}|s_2|^{\beta_{s2}} sgn(s_2) - l_{2,3}|s_2|^{\gamma_{s2}} sgn(s_2) - l_{2,4}s_2 \end{bmatrix} \tag{56}$$

where $\alpha_{si} > 1, 0 < \beta_{si} < 1, l_{i,j} > 0,\ i = 1,2,\ j = 1,2,3,4;$ $sgn(s_i)$ is a signum function. The adaptive law is designed as follows:

$$\begin{cases} \dot{\hat{\theta}}_1 = \Gamma_1 \varphi_1(x_1) z_1 \\ \dot{\hat{\theta}}_2 = \Gamma_2 \varphi_2(x_2) z_2 \\ \dot{\hat{\theta}}_3 = \Gamma_3 \varphi_3(x_3) z_3 \\ \dot{\hat{\theta}}_4 = \Gamma_4 \varphi_4(x_4) S \end{cases} \tag{57}$$

where Γ_i is a symmetric positive definite matrix, $i = 1,\ 2,\ 3,\ 4$.

It can be seen from Equations (49) and (55) that in the ideal cruise process, as long as appropriate parameters are chosen for the control law, the tracking error of the sliding mode system can approach zero, and the desired control signal U^* can be obtained. The ideal desired control signal can be expressed as $U^* = \left[\beta_c^*, \delta_e^*\right]^T = u + d^* = \left[\beta_c + d_{\beta c}^*, \delta_e + d_{\delta e}^*\right]^T$, where $\left[d_{\beta c}^*,\ d_{\delta e}^*\right]^T$ represents interference signal; it can be obtained using Equations (49) and (55) as follows:

$$-z_3 - \sum_{i=1}^{3} c_i \dot{z}_i - f(x,t) - \varphi_4^T(x_4)\hat{\theta}_4 + \dot{\mu}_4 = G(x,t)U^* - u_{sw} \tag{58}$$

Since the actual interference d^* is unknown, this paper uses the RBF neural network to approximate the interference d^* to estimate and compensate for the negative effects of the interference.

3.4. Neural Network Adaptive Control

In this section, an adaptive neural network controller is designed. The interference amount is estimated using the RBF neural network to realize adaptive interference compensation. The RBF network algorithm is represented as follows:

$$h_j = \exp\left(\frac{\left\|x - c_j\right\|^2}{2b_j^2}\right) \tag{59}$$

$$d^* = W^{*T} h(x) + \bar{\varepsilon} \tag{60}$$

where x represents the RBF neural network input, and j represents the jth network input of the hidden layer of the network. $h = \left[h_j\right]^T$ represents the output of the Gaussian basis function; $W^* = \left[W_{\beta c}^*, W_{\delta e}^*\right]^T$ is the ideal weight of the network; $\bar{\varepsilon}$ is an error obtained by an ideal neural network RBF approximating d^*, $\bar{\varepsilon} \le \bar{\varepsilon}_{max}$.

Defining $\hat{W} = \left[\hat{W}_{\beta c}, \hat{W}_{\delta e}\right]^T$ as estimation weights of the RBF neural network W^*, and $\hat{d}$ as neural network output, we obtain the following:

$$\hat{d} = \hat{W}^T h(x) \tag{61}$$

where $\hat{d} = \left[\hat{d}_{\beta_c}, \hat{d}_{\delta_e}\right]^T$. Using $\widetilde{W} = \left[\widetilde{W}_{\beta c}, \widetilde{W}_{\delta e}\right]^T = \hat{W} - W^*$, we obtain the following:

$$d^* - \hat{d} = W^{*T} h(x) + \bar{\varepsilon} - \hat{W}^T h(x) = (W^{*T} - \hat{W}^T) h(x) + \bar{\varepsilon} = -\widetilde{W}^T h(x) + \bar{\varepsilon} \tag{62}$$

where $\bar{\varepsilon}= \left[\bar{\varepsilon}_{\beta c},\ \bar{\varepsilon}_{\delta e}\right]^T$ is an approximation error, meeting the condition $|\bar{\varepsilon}| < E_N$; Since E_N is difficult to determine, E_N can be estimated by $\hat{E}_N(t)$. Then, we obtain the following:

$$\widetilde{E}_N(t) = \hat{E}_N(t) - E_N \tag{63}$$

where $\widetilde{E}_N(t) = \left[\widetilde{E}_{N\beta c}(t), \widetilde{E}_{N\delta e}(t)\right]^T$.

Therefore, the interference estimation based on RBF can be expressed as follows:

$$d = \hat{d} + d_n \tag{64}$$

where $\hat{d}$ is used to estimate the actual disturbance variable d^*; compensation control law $d_n = \left[d_{n(\beta_c)}\ d_{n(\delta_e)}\right]^T$ is used to compensate for the error E_N between d and d^*.

Therefore, by substituting Equation (64) into Equation (55), the adaptive neural network sliding mode backstepping controller is designed as follows:

$$\begin{aligned} u &= G(x,t)^{-1}\left(-z_3 - \sum_{i=1}^{3} c_i \dot{z}_i - f(x,t) - \varphi_4^T(x_4)\hat{\theta}_4 + \dot{\mu}_4 + u_{sw}\right) - d \\ &= G(x,t)^{-1}\left(-z_3 - \sum_{i=1}^{3} c_i \dot{z}_i - f(x,t) - \varphi_4^T(x_4)\hat{\theta}_4 + \dot{\mu}_4 + u_{sw}\right) - \left(\hat{d} + d_n\right) \\ &= G(x,t)^{-1}\left(-z_3 - \sum_{i=1}^{3} c_i \dot{z}_i - f(x,t) - \varphi_4^T(x_4)\hat{\theta}_4 + \dot{\mu}_4 + u_{sw}\right) - \left(\hat{W}^T h(x) + d_n\right) \end{aligned} \tag{65}$$

The neural network adaptive law and compensation control law are designed as follows:

$$\dot{\hat{W}}_{\beta c} = -r_1(s_V b_{11} + s_h b_{21})h \tag{66}$$

$$\dot{\hat{W}}_{\delta e} = -r_2(s_V b_{12} + s_h b_{22})h \tag{67}$$

$$\dot{\hat{E}}_{N\beta_c} = r_3|s_V b_{11} + s_h b_{21}| \tag{68}$$

$$\dot{\hat{E}}_{N\delta_e} = r_4|s_V b_{12} + s_h b_{22}| \tag{69}$$

$$d_{n(\beta_c)} = -\hat{E}_{N\beta_c} sgn(s_V b_{11} + s_h b_{21}) \tag{70}$$

$$d_{n(\delta_e)} = -\hat{E}_{N\delta_e} sgn(s_V b_{12} + s_h b_{22}) \tag{71}$$

4. Stability Analysis and Proof

Theorem 2. *Considering a higher-order nonlinear system with uncertainty and interference described by Equation (25), if the control law of the system is designed as Equation (65), the virtual* *control law is designed as Equation (30), and the adaptive law and compensation control law are designed as Equations (66)–(71), the closed-loop control system is stable.*

Proof of Theorem 2. Considering the effect of interference, Equation (49) can be rewritten as follows:

$$\begin{aligned}\dot{S} &= c_1\dot{z}_1 + c_2\dot{z}_2 + c_3\dot{z}_3 + f(x,t) + G(x,t)[u+d] + \varphi_4^T(x_4)\theta_4 - \dot{\mu}_4 \\ &= c_1\dot{z}_1 + c_2\dot{z}_2 + c_3\dot{z}_3 + f(x,t) + G(x,t)u + \varphi_4^T(x_4)\theta_4 - \dot{\mu}_4 + G(x,t)d\end{aligned} \tag{72}$$

By substituting Equation (58) into Equation (72), we obtain the following:

$$\begin{aligned}\dot{S} &= -z_3 - \varphi_4^T(x_4)\widetilde{\theta}_4 + G(x,t)(d-d^*) + u_{sw} \\ &= -z_3 - \varphi_4^T(x_4)\widetilde{\theta}_4 + \begin{bmatrix} b_{11} & b_{12} \\ b_{21} & b_{22} \end{bmatrix}\begin{bmatrix} \hat{d}_{\beta_c} + d_{n(\beta_c)} - d^*_{\beta c} \\ \hat{d}_{\delta_e} + d_{n(\delta_e)} - d^*_{\delta e} \end{bmatrix} + u_{sw}\end{aligned} \tag{73}$$

The Lyapunov function is defined as:

$$\begin{aligned}L &= V_4 + \frac{1}{2r_1}\widetilde{W}_{\beta c}^T\widetilde{W}_{\beta c} + \frac{1}{2r_2}\widetilde{W}_{\delta_e}^T\widetilde{W}_{\delta_e} + \frac{1}{2r_3}\widetilde{E}_{N\beta c}^T\widetilde{E}_{N\beta c} + \frac{1}{2r_4}\widetilde{E}_{N\delta_e}^T\widetilde{E}_{N\delta_e} \\ &= \frac{1}{2}\sum_{i=1}^{3} k_i z_i^T z_i + \frac{1}{2}\sum_{i=1}^{3}\widetilde{\theta}_i^T\Gamma_i^{-1}\widetilde{\theta}_i + \frac{1}{2}\widetilde{\theta}_4^T\Gamma_4^{-1}\widetilde{\theta}_4 + \frac{1}{2}S^TS \\ &+ \frac{1}{2r_1}\widetilde{W}_{\beta c}^T\widetilde{W}_{\beta c} + \frac{1}{2r_2}\widetilde{W}_{\delta_e}^T\widetilde{W}_{\delta_e} + \frac{1}{2r_3}\widetilde{E}_{N\beta c}^T\widetilde{E}_{N\beta c} + \frac{1}{2r_4}\widetilde{E}_{N\delta_e}^T\widetilde{E}_{N\delta_e}\end{aligned} \tag{74}$$

where $r_i > 0, i = 1,2,3,4$.

Taking the derivative of Equation (74) and substituting Equation (52), we obtain the following:

$$\begin{aligned}\dot{L} &= \frac{1}{2}\sum_{i=1}^{3} k_i z_i^T z_i + \sum_{i=1}^{3}\widetilde{\theta}_i^T\Gamma_i^{-1}\dot{\widetilde{\theta}}_i^T + \widetilde{\theta}_4^T\Gamma_4^{-1}\dot{\widetilde{\theta}}_4 + S^T\dot{S} \\ &+ \frac{1}{r_1}\widetilde{W}_{\beta c}^T\dot{\widetilde{W}}_{\beta c} + \frac{1}{r_2}\widetilde{W}_{\delta_e}^T\dot{\widetilde{W}}_{\delta_e} + \frac{1}{r_3}\widetilde{E}_{\beta c}^T\dot{\widetilde{E}}_{\beta c} + \frac{1}{r_4}\widetilde{E}_{\delta_e}^T\dot{\widetilde{E}}_{\delta_e} \\ &= \sum_{i=1}^{3}[-k_i z_i^T z_i + \widetilde{\theta}_i^T(\varphi_i(x_i)z_i - \Gamma_i^{-1}\dot{\hat{\theta}}_i)] + z_3^T\left(S - \sum_{i=1}^{3} c_i z_i\right) + \widetilde{\theta}_4^T\Gamma_4^{-1}\left(\dot{\theta}_4 - \dot{\hat{\theta}}_4\right) \\ &+ S^T\dot{S} + \frac{1}{r_1}\widetilde{W}_{\beta c}^T\dot{\widetilde{W}}_{\beta c} + \frac{1}{r_2}\widetilde{W}_{\delta_e}^T\dot{\widetilde{W}}_{\delta_e} + \frac{1}{r_3}\widetilde{E}_{\beta c}^T\dot{\widetilde{E}}_{\beta c} + \frac{1}{r_4}\widetilde{E}_{\delta_e}^T\dot{\widetilde{E}}_{\delta_e} \\ &= \sum_{i=1}^{3} -k_i z_i^T z_i - z_3^T\sum_{i=1}^{3} c_i z_i + z_3^T S + \sum_{i=1}^{3}\widetilde{\theta}_i^T[\varphi_i(x_i)z_i - \Gamma_i^{-1}\dot{\hat{\theta}}_i] - \widetilde{\theta}_4^T\Gamma_4^{-1}\dot{\hat{\theta}}_4 \\ &+ S^T\left(-z_3 - \varphi_4^T(x_4)\widetilde{\theta}_4 + \begin{bmatrix} b_{11} & b_{12} \\ b_{21} & b_{22} \end{bmatrix}\begin{bmatrix} \hat{d}_{\beta_c} + d_{n(\beta_c)} - d^*_{\beta c} \\ \hat{d}_{\delta_e} + d_{n(\delta_e)} - d^*_{\delta e} \end{bmatrix} + u_{sw}\right) \\ &+ \frac{1}{r_1}\widetilde{W}_{\beta c}^T\dot{\widetilde{W}}_{\beta c} + \frac{1}{r_2}\widetilde{W}_{\delta_e}^T\dot{\widetilde{W}}_{\delta_e} + \frac{1}{r_3}\widetilde{E}_{\beta c}^T\dot{\widetilde{E}}_{\beta c} + \frac{1}{r_4}\widetilde{E}_{\delta_e}^T\dot{\widetilde{E}}_{\delta_e} \\ &= -z^TQz + \sum_{i=1}^{3}\widetilde{\theta}_i^T[\varphi_i(x_i)z_i - \Gamma_i^{-1}\dot{\hat{\theta}}_i] + \widetilde{\theta}_4^T\left[\varphi_4(x_4)S - \Gamma_4^{-1}\dot{\hat{\theta}}_4\right] \\ &+ S^Tu_{sw} + S^T\begin{bmatrix} b_{11} & b_{12} \\ b_{21} & b_{22} \end{bmatrix}\begin{bmatrix} \hat{d}_{\beta_c} + d_{n(\beta_c)} - d^*_{\beta c} \\ \hat{d}_{\delta_e} + d_{n(\delta_e)} - d^*_{\delta e} \end{bmatrix} \\ &+ \frac{1}{r_1}\widetilde{W}_{\beta c}^T\dot{\widetilde{W}}_{\beta c} + \frac{1}{r_2}\widetilde{W}_{\delta_e}^T\dot{\widetilde{W}}_{\delta_e} + \frac{1}{r_3}\widetilde{E}_{\beta c}^T\dot{\widetilde{E}}_{\beta c} + \frac{1}{r_4}\widetilde{E}_{\delta_e}^T\dot{\widetilde{E}}_{\delta_e}\end{aligned} \tag{75}$$

where

$$\begin{cases} z = \begin{bmatrix} z_1 & z_2 & z_3 \end{bmatrix}^T \\ Q = \begin{bmatrix} k_1 & 0 & 0 \\ 0 & k_2 & 0 \\ c_1 & c_2 & k_3 + c_3 \end{bmatrix} \end{cases} \tag{76}$$

It can be seen from the controller design process that the coefficients k_i and c_i (i=1,2,3) in Q are greater than zero, and the principal minors in matrix Q are greater than zero. Therefore, Q is a positive definite matrix.

After substituting adaptive Equation (57) into Equation (75), we obtain the following:

$$\begin{aligned}
\dot{L} &= -z^TQz + S^Tu_{sw} + S^T\begin{bmatrix} b_{11} & b_{12} \\ b_{21} & b_{22} \end{bmatrix}\begin{bmatrix} \hat{d}_{\beta_c} + d_{n(\beta_c)} - d^*_{\beta c} \\ \hat{d}_{\delta_e} + d_{n(\delta_e)} - d^*_{\delta e} \end{bmatrix} \\
&+\tfrac{1}{r_1}\tilde{W}^T_{\beta c}\dot{\tilde{W}}_{\beta c} + \tfrac{1}{r_2}\tilde{W}^T_{\delta_e}\dot{\tilde{W}}_{\delta_e} + \tfrac{1}{r_3}(\hat{E}_{N\beta c} - E_{N\beta c})\dot{\hat{E}}_{N\beta c} + \tfrac{1}{r_4}(\hat{E}_{N\delta_e} - E_{N\delta_e})\dot{\hat{E}}_{N\delta_e} \\
&= -z^TQz + S^Tu_{sw} + \begin{bmatrix} s_Vb_{11} + s_hb_{21}, s_Vb_{12} + s_hb_{22} \end{bmatrix}\begin{bmatrix} \tilde{W}^T_{\beta c}h - \varepsilon_{N\beta c} + d_{n(\beta_c)} \\ \tilde{W}^T_{\delta e}h - \varepsilon_{N\beta c} + d_{n(\delta_e)} \end{bmatrix} \\
&+\tfrac{1}{r_1}\tilde{W}^T_{\beta c}\dot{\tilde{W}}_{\beta c} + \tfrac{1}{r_2}\tilde{W}^T_{\delta_e}\dot{\tilde{W}}_{\delta_e} + \tfrac{1}{r_3}(\hat{E}_{N\beta c} - E_{N\beta c})\dot{\hat{E}}_{N\beta c} + \tfrac{1}{r_4}(\hat{E}_{N\delta_e} - E_{N\delta_e})\dot{\hat{E}}_{N\delta_e}
\end{aligned} \tag{77}$$

After further sorting out Equation (77), we can obtain the following:

$$\begin{aligned}
\dot{L} &= -z^TQz + S^Tu_{sw} + (s_Vb_{11} + s_hb_{21})\left(\tilde{W}^T_{\beta c}h - \varepsilon_{N\beta c} + d_{n(\beta_c)}\right) \\
&+(s_Vb_{12} + s_hb_{22})\left(\tilde{W}^T_{\delta e}h - \varepsilon_{N\beta c} + d_{n(\delta_e)}\right) \\
&+\tfrac{1}{r_1}\tilde{W}^T_{\beta c}\dot{\tilde{W}}_{\beta c} + \tfrac{1}{r_2}\tilde{W}^T_{\delta_e}\dot{\tilde{W}}_{\delta_e} + \tfrac{1}{r_3}(\hat{E}_{N\beta c} - E_{N\beta c})\dot{\hat{E}}_{N\beta c} + \tfrac{1}{r_4}(\hat{E}_{N\delta_e} - E_{N\delta_e})\dot{\hat{E}}_{N\delta_e} \\
&= -z^TQz + S^Tu_{sw} \\
&+\tilde{W}^T_{\beta c}\left[(s_Vb_{11} + s_hb_{21}\right)h + \tfrac{1}{r_1}\dot{\hat{W}}_{\beta c}\Big] + \tilde{W}^T_{\delta e}\left[(s_Vb_{12} + s_hb_{22})h + \tfrac{1}{r_2}\dot{\hat{W}}_{\delta e}\right] \\
&+(s_Vb_{11} + s_hb_{21})\left(-\varepsilon_{N\beta c} + d_{n(\beta_c)}\right) + (s_Vb_{12} + s_hb_{22})\left(-\varepsilon_{N\delta e} + d_{n(\delta_e)}\right) \\
&+\tfrac{1}{r_3}(\hat{E}_{N\beta c} - E_{N\beta c})\dot{\hat{E}}_{N\beta c} + \tfrac{1}{r_4}(\hat{E}_{N\delta_e} - E_{N\delta_e})\dot{\hat{E}}_{N\delta_e}
\end{aligned} \tag{78}$$

According to Lyapunov stability theory, in order to guarantee stability of the system, $\dot{L} < 0$ is needed to be ensured in Equation (78). By substituting the adaptive Equations (66)–(71) into Equation (78), we obtain the following:

$$\begin{aligned}
\dot{L} &= -z^TQz - \sum_{i=1}^{2}\left(l_{i,1}|s_i|^{\alpha_{si}+1} + l_{i,2}|s_i|^{\beta_{si}+1} + l_{i,3}|s_i|^{\gamma_{si}+1} + l_{i,4}s^2\right) \\
&-\varepsilon_{N\beta c}(s_Vb_{11} + s_hb_{21}) - E_{N\beta c}|s_Vb_{11} + s_hb_{21}| \\
&-\varepsilon_{N\delta e}(s_Vb_{12} + s_hb_{22}) - E_{N\delta_e}|s_Vb_{12} + s_hb_{22}| \\
&\le -z^TQz - \sum_{i=1}^{2}\left(l_{i,1}|s_i|^{\alpha_{si}+1} + l_{i,2}|s_i|^{\beta_{si}+1} + l_{i,3}|s_i|^{\gamma_{si}+1} + l_{i,4}s^2\right) \\
&+|\varepsilon_{N\beta c}||s_Vb_{11} + s_hb_{21}| - E_{N\beta c}|s_Vb_{11} + s_hb_{21}| \\
&+|\varepsilon_{N\delta e}||s_Vb_{12} + s_hb_{22}| - E_{N\delta_e}|s_Vb_{12} + s_hb_{22}| \\
&= -z^TQz - \sum_{i=1}^{2}\left(l_{i,1}|s_i|^{\alpha_{si}+1} + l_{i,2}|s_i|^{\beta_{si}+1} + l_{i,3}|s_i|^{\gamma_{si}+1} + l_{i,4}s^2\right) \\
&+(|\varepsilon_{N\beta c}| - E_{N\beta c})|s_Vb_{11} + s_hb_{21}| + (|\varepsilon_{N\delta e}| - E_{N\delta_e})|s_Vb_{12} + s_hb_{22}| \\
&< -z^TQz - \sum_{i=1}^{2}\left(l_{i,1}|s_i|^{\alpha_{si}+1} + l_{i,2}|s_i|^{\beta_{si}+1} + l_{i,3}|s_i|^{\gamma_{si}+1} + l_{i,4}s^2\right) \le 0
\end{aligned} \tag{79}$$

The proof is completed. □

5. Simulation of NMV Cruise Flight Controller Based on Adaptive Neural Network Sliding Mode Backstepping Control

5.1. Simulation 1: Simulation of Reaching Laws

In order to verify the superiority of the approach law proposed in this paper, a traditional sliding mode controller [31] is used in this section to track the speed of NMV. The sliding mode surface adopted in this simulation is defined as follows [31]:

$$s_h = \left(\frac{d}{dt} + \lambda_h\right)^4 \int_0^t e(\tau)dt \tag{80}$$

Five different reaching laws are compared and analyzed by simulation, including enhanced triple reaching law (ETPRL), triple reaching law (TPRL), double power reaching law (DPRL), exponential reaching law (ERL), and traditional symbolic function reaching law (TRL). The expressions of the five approach laws are as follows:

(1) ETPRL:

$$-l_1|s_h|^{\alpha_s} sgn(s_h) - l_2|s_h|^{\beta_s} sgn(s_h) - l_3|s_h|^{\gamma_s} sgn(s_h) - l_4 s_h \tag{81}$$

(2) TPRL:

$$-l_1|s_h|^{\alpha_s} sgn(s_h) - l_2|s_h|^{\beta_s} sgn(s_h) - l_3|s_h|^{\gamma_s} sgn(s_h) \tag{82}$$

(3) DPRL:

$$-l_1|s_h|^{\alpha_s} sgn(s_h) - l_2|s_h|^{\beta_s} sgn(s_h) \tag{83}$$

(4) ERL:

$$-l_1 sgn(s_h) - l_2 s_h \tag{84}$$

(5) TRL:

$$-l_1 sgn(s_h) \tag{85}$$

Simulation parameters of different reaching laws are shown in Table 2.

Table 2. Parameters for Reaching laws.

ETPRL	TPRL	DPRL	ERL	TRL
$l_1 = 1$	$l_1 = 1$	$l_1 = 1$	$l_1 = 1$	$l_1 = 1$
$l_2 = 1$	$l_2 = 1$	$l_2 = 1$	$l_2 = 1$	
$l_3 = 0.5$	$l_3 = 0.5$	$\alpha_s = 1.3$		
$l_4 = 0.5$	$\alpha_s = 1.3$	$\beta_s = 0.7$		
$\alpha_s = 1.3$	$\beta_s = 0.7$			
$\beta_s = 0.7$	$\delta = 1.8$			
$\delta = 1.8$	$\omega = 2$			
$\omega = 2$				

NMV model parameters are shown in Table 3.

Table 3. Model parameters of NMV with winglet stretching.

Parameter	Value	Units
Mass	100,200	kg
Reference area	389	m^2
Aerodynamic chord	30	m
Moment of inertia	8,466,900	$kg{\cdot}m^2$

In the simulation, NMV is in the cruise phase and its initial state is assumed to be: $h_0 = 34,950$ m, $V_0 = 3310$ m/s, $\gamma = 0^{\circ}$, $\alpha = 2.745^{\circ}$, and $q = 0^{\circ}$/s, and the height command signal is a step input of 100 m. The elevator control efficiency of the control input channel δ_e is set to be 30% lower than expected: $\delta_e = \delta_{e0} \times 0.7$. In order to improve flight lift, NMV winglets are kept stretched.

The simulation results are shown in Figures 6–8.

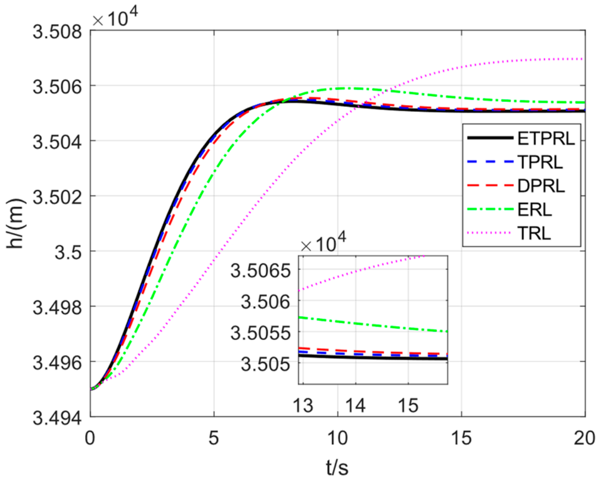

Figure 6. Height response curve.

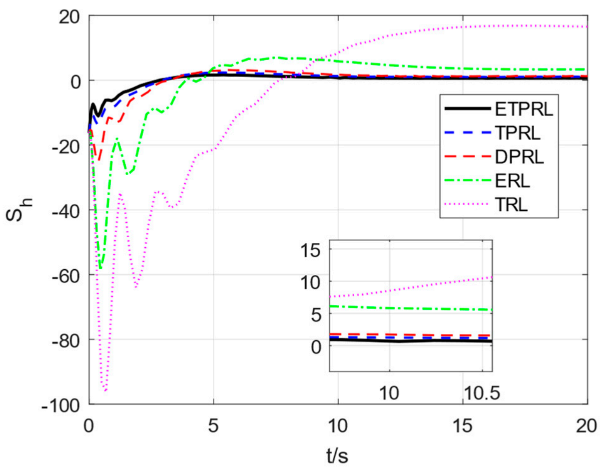

Figure 7. Response curve of S_h.

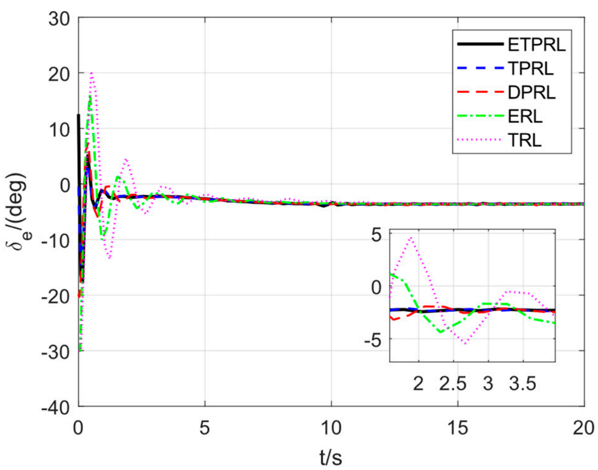

Figure 8. The response curve of the control input δ_e.

As can be seen from Figure 6, compared with the other four reaching laws, ETPRL, the reaching law proposed in this paper, can ensure that the height of the aircraft reaches the steady state in the shortest time. In Figure 7, compared with the other four reaching rules, the sliding mode surface s_h can approach the zero equilibrium point in the shortest time under ETPRL. As seen in Figure 8, the control input has a larger chattering under TRL and ERL, while the chattering of the system is suppressed under ETPRL. This is because $-l_1 sgn(S_h)$ is contained in both TRL and ERL expressions, while it is not included in ETPRL expressions. The above analysis shows that compared with the other four reaching laws, the ETPRL reaching law proposed in this paper can ensure that the system converges to the equilibrium point in the shortest time and reduces the chattering when the elevator control efficiency decreases greatly. Therefore, ETPRL can achieve a faster-reaching speed than the other four approach laws, and can effectively weaken the negative impact of the decline of elevator control efficiency on NMV during the cruise phase.

5.2. Scenario 2: Simulation Verification of NMV Cruising Level Flight Acceleration Mode

In this scenario, the fuzzy sliding mode dynamic surface control based on a neural network is adopted in the control scheme. NMV flight in patrol mode, of which the initial state is $V_0 = 3310$ m/s, $h_0 = 34{,}950$ m, $\gamma = 0^{\circ}$, $\alpha = 1.9^{\circ}$, and $q = 0^{\circ}/s$. In order to improve flight efficiency, in the level flight acceleration mode, the NMV winglets are retracted to reduce flight drag. Compared with winglet stretching, the wing reference area and aerodynamic chord length of NMV become smaller when winglets retract. The model parameters of NMV in flat flight acceleration mode are shown in Table 4.

Table 4. Model parameters of NMV with winglets retracting.

Parameter	Value	Unites
Mass	100,200	kg
Reference area	369	m^2
Aerodynamic chord	27	m
Moment of inertia	8,466,900	$kg{\cdot}m^2$

In the simulation of this section, Equation (65) is adopted for the controller, Equation (30) for the virtual control law, Equation (56) for the sliding mode reaching law, Equation (57) for the adaptive law, and Equations (66)–(71) for the neural network adaptive law and compensation control law. Table 5 shows the values of controller parameters.

The simulation instruction signal of the level flight acceleration mode is set as follows: (i) the height of the NMV remains unchanged, and (ii) $V_d(t) = V_0 + \Delta V(t)$; $\Delta V(t)$ is generated by the filter of the step input, which is set as follows:

$$\frac{\Delta V(s)}{V_{step}(s)} = \frac{0.3^2}{(s+0.3)^2} \tag{86}$$

where the speed step instruction is set as $V_{step} = 100$ m/s. In the control input $u = \begin{bmatrix} \beta_c & \delta_e \end{bmatrix}^T$, the threshold value range of β_c is from 0 to 2, while the threshold value range of δ_e is $\pm 30^{\circ}$. In the cruising mode, due to the decline of elevator control efficiency and uncertainty for the NMV, the change of elevator control efficiency and uncertainties for the NMV in the simulation are set as follows:

(1) Elevator control efficiency of control input channel δ_e is set for a 30% drop in value than expected;

$$\begin{cases} \delta_e = \delta_{e0} \times 0.7 + 0.1 sin(0.02\pi t) \\ \beta_c = \beta_{c0} + 0.05 sin(0.02\pi t) \end{cases} \tag{87}$$

(2) The maximum uncertainty is set to 10% of the nominal value of each parameter, which is $|\Delta_i| \leq 0.1$ and expressed as follows:

$$i = i_0(1 + 0.1sin(0.02\pi t)) \quad (88)$$

where $i = m, I_{yy}, \rho, s_w, \ \bar{c}, c_e, C_L, C_D, C_T, C_M^\alpha, C_M^q, C_M^{\delta_e}$.

Table 5. Controller parameters for the cruising level acceleration mode.

Parameter	Value
k_1	$\begin{bmatrix} 0.1 & 0 \\ 0 & 0.1 \end{bmatrix}$
k_2	$\begin{bmatrix} 0.2 & 0 \\ 0 & 0.2 \end{bmatrix}$
k_3	$\begin{bmatrix} 0.1 & 0 \\ 0 & 0.1 \end{bmatrix}$
c_1	$\begin{bmatrix} 1 & 0 \\ 0 & 1 \end{bmatrix}$
c_2	$\begin{bmatrix} 5 & 0 \\ 0 & 5 \end{bmatrix}$
c_3	$\begin{bmatrix} 5 & 0 \\ 0 & 5 \end{bmatrix}$
$l_{1,1}$	1
$l_{1,2}$	1
$l_{1,3}$	0.5
$l_{1,4}$	0.5
$l_{2,1}$	1
$l_{2,2}$	1
$l_{2,3}$	0.5
$l_{2,4}$	0.5
r_1	0.1
r_2	0.2
r_3	0.04
r_4	0.03

In the simulation, in order to verify that the proposed method can achieve better flight performance in the level flight acceleration mode, the proposed method is compared with two other control schemes: one is the traditional double-power approach law sliding mode control (SMC); the other is backstepping sliding mode control (BSMC) which adopts the traditional double power reaching law. Figures 9–16 show the simulation results.

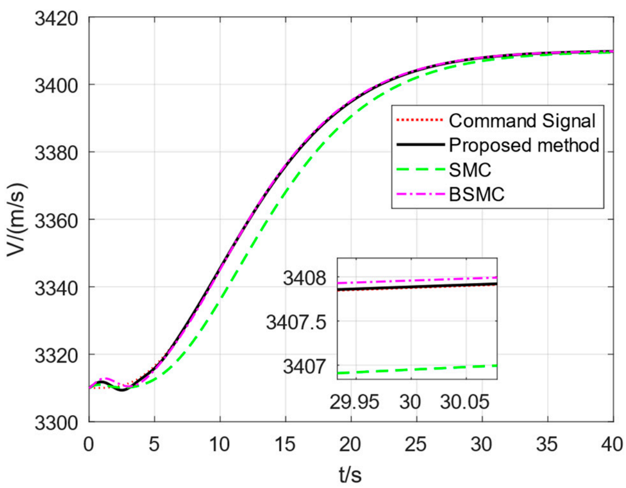

Figure 9. Responses of velocity tracking.

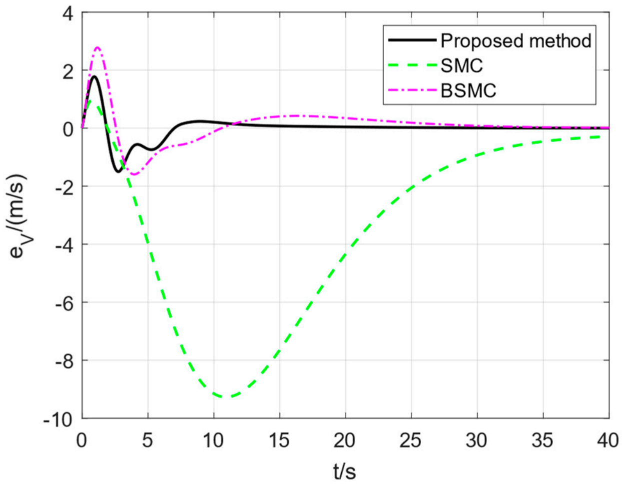

Figure 10. Tracking errors of velocity.

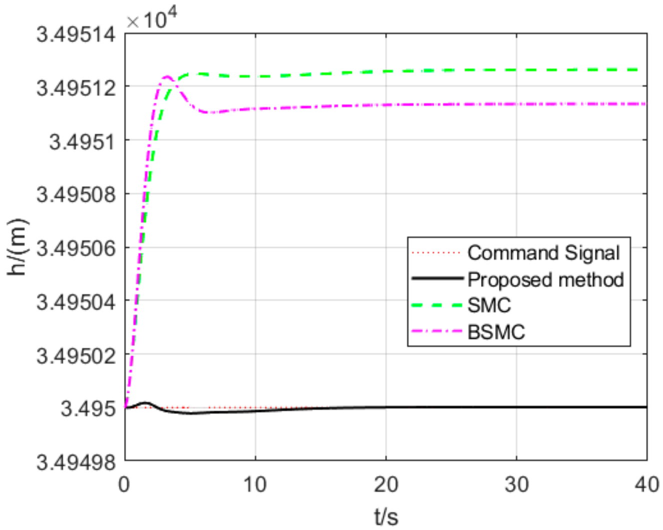

Figure 11. Responses of altitude tracking.

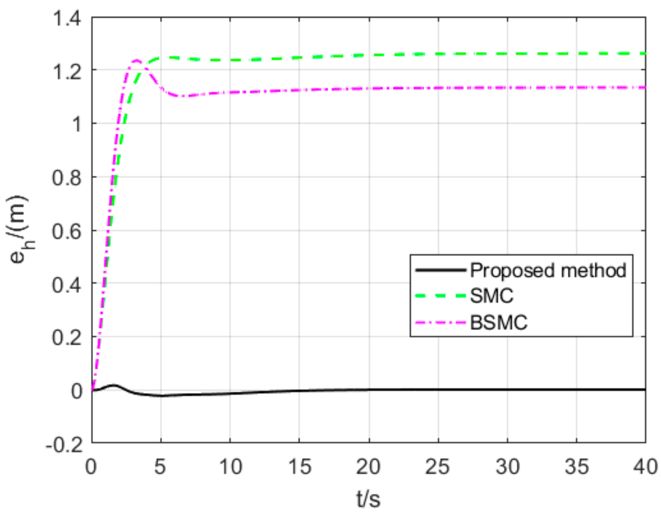

Figure 12. Tracking errors of altitude.

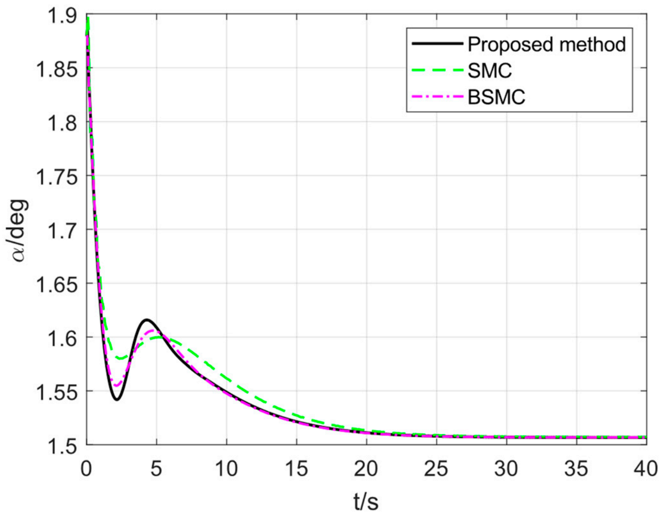

Figure 13. Responses of attack angle.

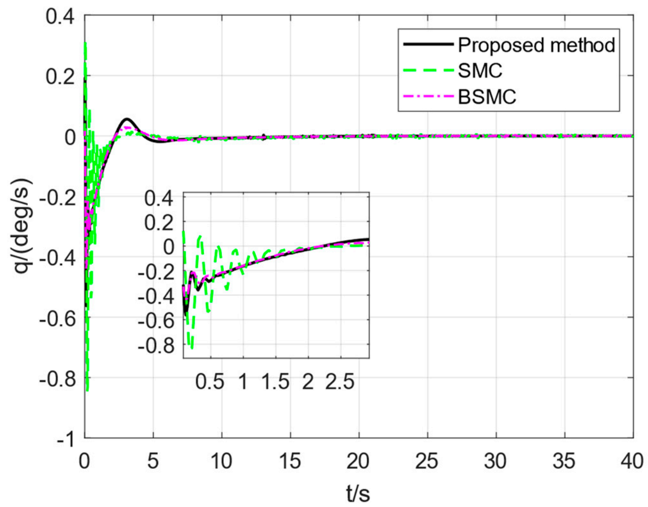

Figure 14. Responses of pitch angle rate.

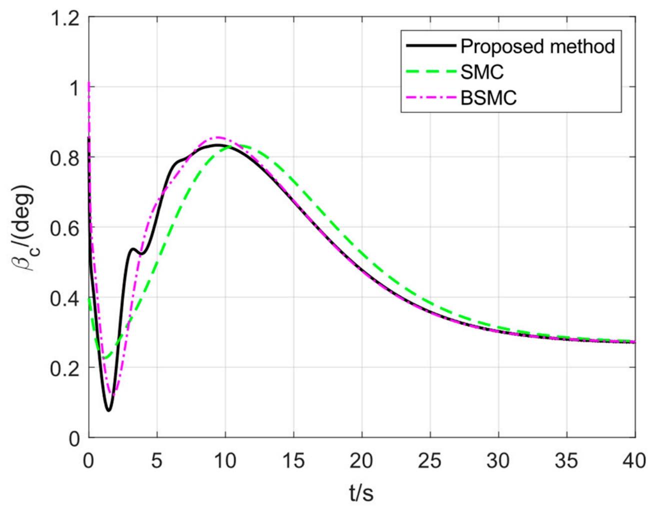

Figure 15. Responses of engine throttle setting.

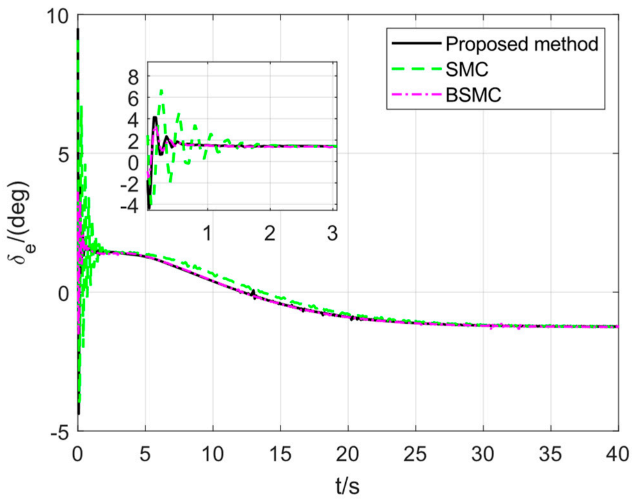

Figure 16. Responses of elevator deflection.

As seen in Figures 9 and 10, the maximum speed tracking error for the method adopted in this paper is 1.8 m/s, and the speed tracking error approaches 0 at 12 s. In comparison, the maximum speed tracking errors for SMC and BSMC are 2.5 m/s and 9 m/s, respectively, and the speed tracking errors approach 0 in 30 s and 40 s, respectively. In addition, Figures 11 and 12 show that the height tracking error of the method adopted in this paper is at most 0.1 m and approaches 0 at the 11th second. Whereas, the height tracking errors of SMC and BSMC are 1.21 m and 1.25 m, respectively, but the height tracking errors for both cannot converge to 0. Therefore, compared with SMC and BSMC, the proposed method has the smallest velocity tracking error and height tracking error. It can be seen from Figures 13 and 14 that variations of both the angle of attack and pitch angle rate of the aircraft for the method proposed in this paper are within reasonable ranges. Both Figures 15 and 16 show the output responses of the NMV controller. It can be seen that both the engine throttle setting value and the response curve of the elevator change steadily and fluctuate within the threshold range. By contrast, the elevator chatters violently during the initial phase for SMC.

According to the analysis of the above simulation results, the following conclusions can be drawn: (i) Compared with SMC and BSMC, the proposed method can make the flight control system have better altitude and velocity tracking accuracy under the level flight acceleration mode. First, the altitude and speed tracking errors of the flight control system proposed in this paper are smaller than those in SMC or BSMC. Second, the response of attack angle and pitch angle rate for the method used in this paper changes more smoothly. Third, the control input for the method proposed in this paper changes smoothly and within an acceptable range. Therefore, compared with BSMC and SMC, the flight control system under the proposed method has better flight performance. (ii) Under the level flight acceleration mode, the method proposed in this paper can effectively reduce the adverse influence of decreasing elevator control efficiency and uncertainty on NMV. The tracking error of the proposed method is smaller than that of SMC and BSMC; furthermore, the tracking error could approach 0 in a shorter time. In addition, the proposed method can abate the chattering of the control input of the flight system. Therefore, the method proposed in this paper can effectively compensate for the influence of uncertainty and can reduce the adverse effect of decreasing elevator control efficiency on NMV under the level flight acceleration mode.

5.3. Scenario 3: Simulation Verification of NMV Cruise Altitude Climbing Mode

In this scenario, the sliding mode backward step control method based on a neural network is adopted in the control scheme. NMV flight in the cruising phase, of which the initial state is $V_0 = 3310$ m/s, $h_0 = 35,500$ m, $\gamma = 0^\circ$, $\alpha = 0.8^\circ$, and $q = 0^\circ$/s. In the altitude climbing mode, in order to increase the lift coefficient, the winglets of NMV remain stretching. The model parameters of NMV are shown in Table 2 above. The simulation command signal is set as follows:$h_d(t) = h_0 + \Delta h(t)$; $\Delta h(t)$ is generated by a step input filter, which is set as follows:

$$\frac{\Delta h(s)}{h_{step}(s)} = \frac{0.3^2}{(s+0.3)^2} \tag{89}$$

where height step instruction is set as $h_{step} = 500$ m. In the control input $u = \begin{bmatrix} \beta_c & \delta_e \end{bmatrix}^T$, the threshold value range of β_c is from 0 to 2, while the threshold value range of δ_e is $\pm 30°$. In the cruising mode, due to the decline in elevator control efficiency and uncertainty for the NMV, the setting on the change of elevator control efficiency and the uncertainty for the NMV in the simulation are similar to that of simulation 2, namely the following:

(i) Elevator control efficiency of control input channel δ_e is set for a 30% drop in value than expected;

$$\begin{cases} \delta_e = \delta_{e0} 0.7 + 0.1 sin(0.02\pi t) \\ \beta_c = \beta_{c0} + 0.05 sin(0.02\pi t) \end{cases} \tag{90}$$

(ii) The maximum uncertainty is set to 10% of the nominal value of each parameter, which is $|\Delta_i| \leq 0.1$ and expressed as follows:

$$i = i_0(1 + 0.1 sin(0.02\pi t)) \tag{91}$$

where $i = m, I_{yy}, \rho, s_w, \bar{c}, c_e, C_L, C_D, C_T, C_M^{\alpha}, C_M^{q}, C_M^{\delta_e}$.

Equation (65) is adopted for the controller, Equation (30) for the virtual control law, Equation (57) for the adaptive law, Equation (56) for the sliding mode reaching law, and Equations (66)–(71) for the neural network adaptive law and compensation control law. Table 6 shows the values of controller parameters.

Table 6. Controller parameters for cruise altitude climbing mode.

Parameter	Value
k_1	$\begin{bmatrix} 0.1 & 0 \\ 0 & 0.1 \end{bmatrix}$
k_2	$\begin{bmatrix} 0.2 & 0 \\ 0 & 0.2 \end{bmatrix}$
k_3	$\begin{bmatrix} 0.3 & 0 \\ 0 & 0.3 \end{bmatrix}$
c_1	$\begin{bmatrix} 1 & 0 \\ 0 & 1 \end{bmatrix}$
c_2	$\begin{bmatrix} 5 & 0 \\ 0 & 5 \end{bmatrix}$
c_3	$\begin{bmatrix} 5 & 0 \\ 0 & 5 \end{bmatrix}$
$l_{1,1}$	1
$l_{1,2}$	1
$l_{1,3}$	0.5
$l_{1,4}$	0.5
$l_{2,1}$	1
$l_{2,2}$	1
$l_{2,3}$	0.5
$l_{2,4}$	0.5
r_1	0.1
r_2	0.2
r_3	0.04
r_4	0.03

In the simulation, the proposed method is compared with traditional sliding mode control (SMC) and backstepping sliding mode control (BSMC) in order to verify that the aircraft can achieve better flight performance in the altitude climbing mode controlled by the proposed method. Figures 17–24 show the simulation results.

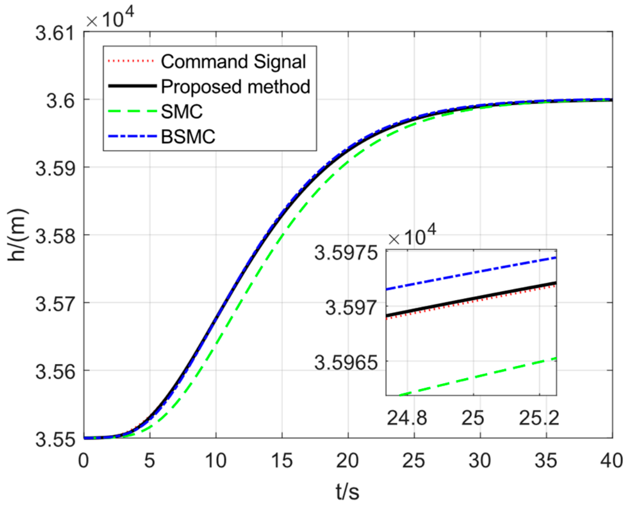

Figure 17. Responses of altitude tracking.

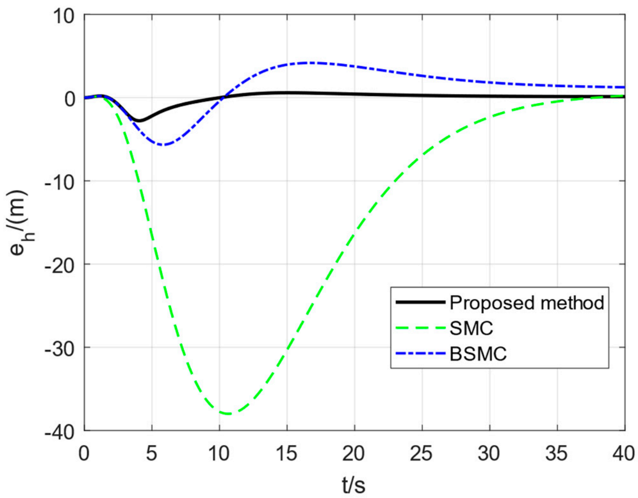

Figure 18. Tracking errors of altitude.

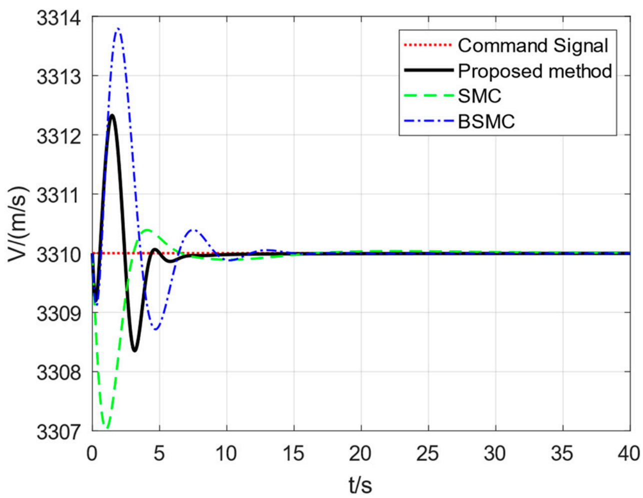

Figure 19. Responses of velocity tracking.

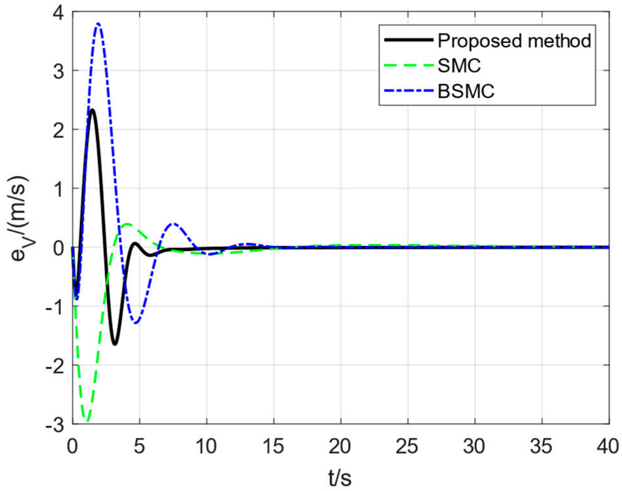

Figure 20. Tracking errors of velocity.

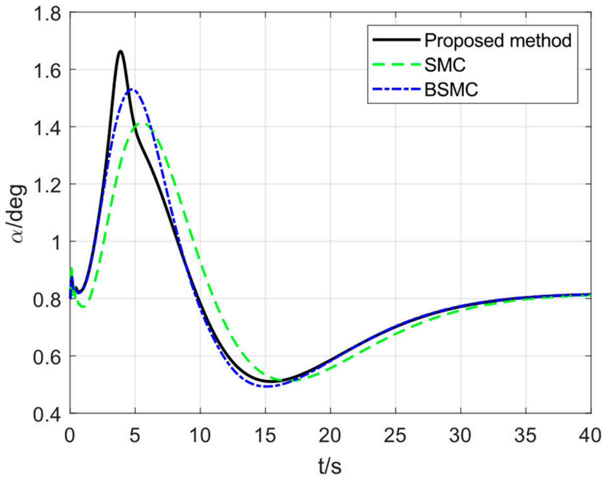

Figure 21. Responses of attack angle.

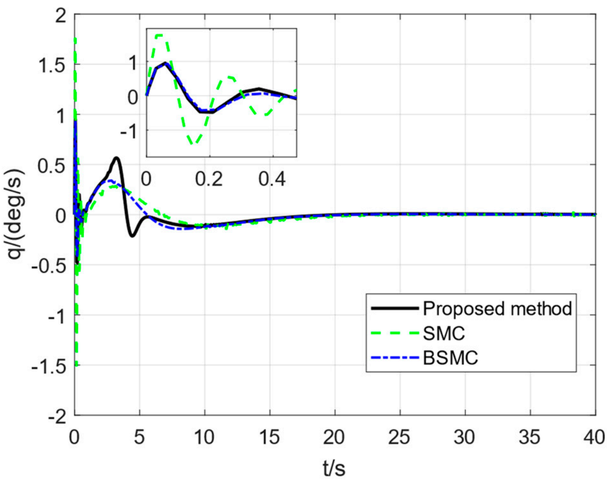

Figure 22. Responses of pitch angle rate.

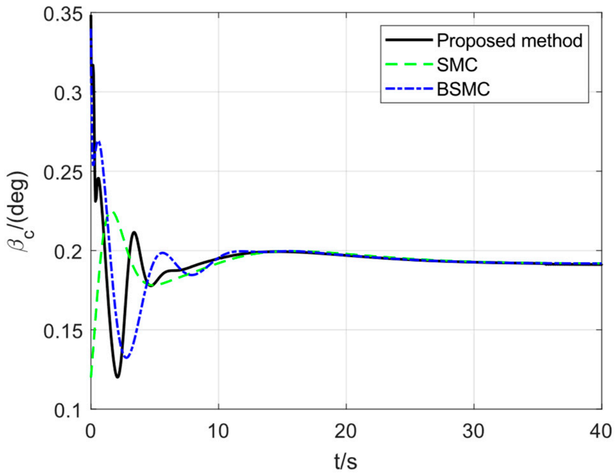

Figure 23. Responses of engine throttle setting.

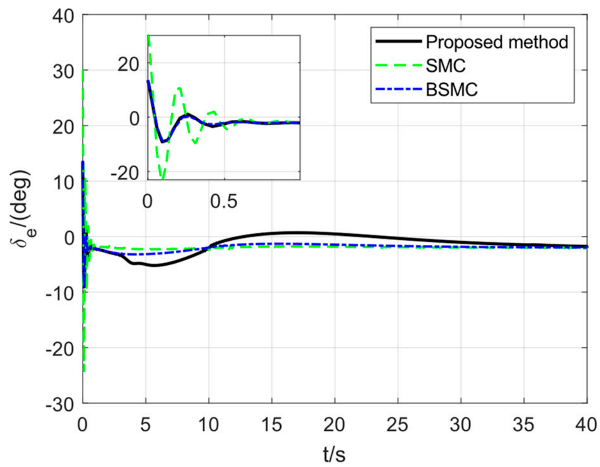

Figure 24. Responses of elevator deflection.

It can be seen from Figures 17 and 18 that the maximum altitude tracking error for the method proposed in this paper is 2 m and approaches 0 at the ninth second. Whereas, the maximums of altitude tracking error of SMC and BSMC are 38 m and 6 m, respectively, and approach 0 around 35 and 40 s, respectively. As can be seen from Figures 19 and 20, the maximum velocity tracking error for the proposed method appears in the initial stage, with the maximum error being 2.3 m/s and the error approaching 0 at the seventh second. By contrast, the velocity tracking errors of SMC and BSMC are 3 m and 3.8 m, respectively. Therefore, it can be seen that compared with SMC and BSMC, altitude tracking error and velocity tracking error of the aircraft are the smallest under the proposed method, and the convergence time is the shortest. It can be seen from Figures 23 and 24 that for the method proposed in this paper, both engine throttle setting and elevator deflection angle change steadily and fluctuate within the threshold range. However, the elevator deflection angle for SMC reaches the threshold in the initial stage, and large chattering occurs.

According to the analysis of the above simulation results, the following conclusions can be drawn: (i) compared with SMC and BSMC, the aircraft in the altitude climbing mode exhibits better tracking performance under the proposed method. Firstly, the altitude and velocity tracking errors of the flight control system in the method proposed in this paper are smaller than those in SMC or BSMC, and the error can approach 0 in a much shorter time. Secondly, the attack angle and pitch angle rate for the method used in this paper change more smoothly. Thirdly, the control input for the method proposed in this paper changes smoothly and within an acceptable range. Therefore, compared with BSMC and SMC, the flight control system under the proposed method obtains better flight performance.

(ii) Under the altitude climbing mode, the adverse influence of decreasing elevator control efficiency and uncertainty on NMV could be reduced effectively by the method proposed in this paper. Considering that the decrease of elevator control efficiency and uncertainty have greater negative impacts on the altitude and velocity tracking of aircraft, the proposed method effectively could reduce the tracking error and shorten the convergence time of both altitude and velocity tracking errors, compared with SMC and BSMC. Therefore, the method proposed in this paper can effectively weaken the adverse effects of decreasing elevator control efficiency and uncertainty on NMV in cruise altitude climbing mode.

6. Conclusions

In this paper, to solve the issues of decreasing elevator control efficiency and uncertainties in the NMV cruise phase, an adaptive sliding mode backstepping control scheme based on a neural network is proposed. Firstly, we analyzed the changes in aerodynamic parameters of NMV in the state of winglet stretching and retracting, and found that NMV can improve the flight efficiency in the cruise phase by retracting winglets in the level flight mode and stretching winglets in the altitude climbing mode. Secondly, an enhanced triple power reaching law (ETPRL) is proposed to ensure that the sliding mode control system can converge quickly and reduce chattering. Thirdly, considering the advantages of backstepping control in nonlinear system control and sliding mode control in robust control, the above two control methods were merged to ensure that the control system can track the command signal stably. And, adaptive control laws were developed to adaptively compensate for the negative effects of parameter uncertainty. In addition, to solve the problem of decreasing elevator control efficiency in the cruise phase and improving tracking accuracy and robustness of the NMV, an adaptive neural network was used to estimate and compensate for the interference on the control channel. Numerical simulation results verify the effectiveness of the proposed control method.

Author Contributions: Conceptualization, S.H.; methodology, S.H.; software, S.H.; validation, S.H.; formal analysis, O.L.; investigation, S.H. and O.L.; resources, S.H. and J.J.; data curation, S.H.; writing—original draft preparation, S.H.; writing—review and editing, S.H. All authors have read and agreed to the published version of the manuscript.

Funding: This research was funded by the National Natural Science Foundation of China, grant number 61966010 and 61673209.

Institutional Review Board Statement: Not applicable for studies not involving humans or animals.

Informed Consent Statement: Not applicable for studies not involving humans or animals.

Data Availability Statement: The data presented in this study are available on request from the corresponding author.

Conflicts of Interest: The authors declare no conflict of interest.

References

1. Sziroczak, D.; Smith, H. A review of design issues specific to hypersonic flight vehicles. *Prog. Aerosp. Sci.* **2016**, *84*, 1–28. [CrossRef]
2. Jiao, X.; Fidan, B.; Jiang, J.; Kamel, M. Adaptive mode switching of hypersonic morphing aircraft based on type-2 TSK fuzzy sliding mode control. *Sci. China Inform. Sci.* **2015**, *58*, 1–15. [CrossRef]
3. Hu, Q.; Wang, C.; Li, Y.; Huang, J. Adaptive control for hypersonic vehicles with time-varying faults. *IEEE Trans. Aerosp. Electron. Syst.* **2018**, *54*, 1442–1455. [CrossRef]
4. Zhao, K.; Song, J.; Ai, S.; Xu, X.; Liu, Y. Active Fault-Tolerant Control for Near-Space Hypersonic Vehicles. *Aerospace* **2022**, *9*, 237. [CrossRef]
5. Dong, M.; Xu, X.; Xie, F. Constrained Integrated Guidance and Control Scheme for Strap-Down Hypersonic Flight Vehicles with Partial Measurement and Unmatched Uncertainties. *Aerospace* **2022**, *9*, 840. [CrossRef]
6. Zong, Q.; Ji, Y.; Zeng, F.; Liu, H. Output feedback back-stepping control for a generic hypersonic vehicle via small-gain theorem. *Aerosp. Sci. Technol.* **2012**, *23*, 409–417. [CrossRef]
7. Shao, K.; Wan, Z.; Yang, C. Control surfaces efficiency analysis of flexible aircraft based on experimental aerodynamic forces. *Acta Aeronaut. Astronaut. Sin.* **2009**, *30*, 1612–1617.

8. Sun, J.; Yi, J.; Pu, Z.; Liu, Z. Adaptive fuzzy nonsmooth backstepping output-feedback control for hypersonic vehicles with finite-time convergence. *IEEE Trans. Fuzzy Syst.* **2020**, *28*, 2320–2334. [CrossRef]
9. Tang, X.; Zhai, D.; Li, X. Adaptive fault-tolerance control based finite-time backstepping for hypersonic flight vehicle with full state constrains. *Inform. Sci.* **2020**, *507*, 53–66. [CrossRef]
10. Sun, J.; Yi, J.; Pu, Z.; Tan, X. Fixed-time sliding mode disturbance observer-based nonsmooth backstepping control for hypersonic vehicles. *IEEE Trans. Syst. Man Cybern. Syst.* **2020**, *50*, 4377–4386. [CrossRef]
11. Lu, Y. Disturbance observer-based backstepping control for hypersonic flight vehicles without use of measured flight path angle. *Chin. J. Aeronaut.* **2021**, *34*, 396–406. [CrossRef]
12. Hu, Q.; Meng, Y.; Wang, C.; Zhang, Y. Adaptive backstepping control for air-breathing hypersonic vehicles with input nonlinearities. *Aerosp. Sci. Technol.* **2018**, *73*, 289–299. [CrossRef]
13. Zhang, S.; Wang, Q.; Yang, G.; Zhang, M. Anti-disturbance backstepping control for air-breathing hypersonic vehicles based on extended state observer. *ISA Trans.* **2019**, *92*, 84–93. [CrossRef] [PubMed]
14. Zhang, X.; Zong, Q.; Dou, L.; Tian, B.; Liu, W. Improved finite-time command filtered backstepping fault-tolerant control for flexible hypersonic vehicle. *J. Frankl. Inst.* **2020**, *357*, 8543–8565. [CrossRef]
15. Yaseen, H.M.S.; Siffat, S.A.; Ahmad, I.; Malik, A.S. Nonlinear adaptive control of magnetic levitation system using terminal sliding mode and integral backstepping sliding mode controllers. *ISA Trans.* **2022**, *126*, 121–133. [CrossRef]
16. Ding, Y.; Wang, X.; Bai, Y.; Cui, N. An improved continuous sliding mode controller for flexible air-breathing hypersonic vehicle. *Int. J. Robust Nonlinear Control* **2020**, *30*, 5751–5772. [CrossRef]
17. Basin, M.V.; Yu, P.; Shtessel, Y.B. Hypersonic missile adaptive sliding mode control using finite- and fixed-time observers. *IEEE Trans. Ind. Electron.* **2018**, *65*, 930–941. [CrossRef]
18. Zhang, Y.; Ma, G.; Guo, Y.; Zeng, T. A multi power reaching law of sliding mode control design and analysis. *Acta Autom. Sin.* **2016**, *42*, 466–472.
19. Zhang, H.; Fan, J.; Meng, F.; Huang, J. A new double power reaching law for sliding mode control. *Control Decis.* **2013**, *28*, 289–293.
20. Zhou, T. Adaptive sliding control based on a new reaching law. *Control Decis.* **2016**, *31*, 1335–1338.
21. Dai, P.; Xu, N.; Xie, H.; Lü, Y. PMSM sliding mode control based on fast power reaching law. *Electr. Mach. Control* **2017**, *21*, 32–38.
22. Mozayan, S.M.; Saad, M.; Vahedi, H.; Fortin-Blanchette, H.; Soltani, M. Sliding mode control of PMSG wind turbine based on enhanced exponential reaching law. *IEEE Trans. Ind. Electron.* **2016**, *63*, 6148–6159. [CrossRef]
23. Wei, Q.; Shi, G.; Song, R.; Liu, Y. Adaptive dynamic programming-based optimal control scheme for energy storage systems with solar renewable energy. *IEEE Trans. Ind. Electron.* **2017**, *64*, 5468–5478. [CrossRef]
24. Sagliano, M.; Mooij, E.; Theil, S. Adaptive disturbance-based high-order sliding-mode control for hypersonic-entry vehicles. *J. Guid. Control Dyn.* **2017**, *40*, 521–536. [CrossRef]
25. Yu, C.; Jiang, J.; Zhen, Z.; Bhatia, A.K.; Wang, S. Adaptive backstepping control for air-breathing hypersonic vehicle subject to mismatched uncertainties. *Aerosp. Sci. Technol.* **2020**, *107*, 106244. [CrossRef]
26. Bu, X.; Lei, H. A fuzzy wavelet neural network-based approach to hypersonic flight vehicle direct nonaffine hybrid control. *Nonlinear Dynam.* **2018**, *94*, 1657–1668. [CrossRef]
27. Dai, P.; Feng, D.; Feng, W.; Cui, J.; Zhang, L. Entry trajectory optimization for hypersonic vehicles based on convex programming and neural network. *Aerosp. Sci. Technol.* **2023**, *137*, 108259. [CrossRef]
28. An, H.; Guo, Z.; Wang, G.; Wang, C. Neural adaptive control of air-breathing hypersonic vehicles robust to actuator dynamics. *ISA Trans.* **2021**, *116*, 17–29. [CrossRef]
29. Gao, D.; Wang, S.; Zhang, H. A singularly perturbed system approach to adaptive neural back-stepping control design of hypersonic vehicles. *J. Intell. Robot. Syst.* **2014**, *73*, 249–259. [CrossRef]
30. Xia, R.; Chen, M.; Wu, Q.; Wang, Y. Neural network based integral sliding mode optimal flight control of near space hypersonic vehicle. *Neurocomputing* **2020**, *379*, 41–52. [CrossRef]
31. Jiao, X.; Jiang, J. Design of adaptive switching control for hypersonic aircraft. *Adv. Mech. Eng.* **2015**, *7*, 1–10. [CrossRef]
32. Xu, H.; Mirmirani, M.D.; Ioannou, P.A. Adaptive sliding mode control design for a hypersonic flight vehicle. *J. Guid. Control Dyn.* **2004**, *27*, 829–838. [CrossRef]
33. Zhang, Y.; Li, R.; Xue, T.; Lei, Z. Exponential sliding mode tracking control via back-stepping approach for a hypersonic vehicle with mismatched uncertainty. *J. Frankl. Inst.* **2016**, *353*, 2319–2343. [CrossRef]